

AUS Repository

Computational Fluid Dynamics of Energy Separation in Vortex Tube

Item Type	Thesis
Authors	Al Saghir, Ahmad Mohammad
Download date	2026-04-16 10:36:52
Link to Item	http://hdl.handle.net/11073/21534

COMPUTATIONAL FLUID DYNAMICS OF ENERGY

SEPARATION IN VORTEX TUBE

by
Ahmad Mohammad Al Saghir

A Thesis presented to the Faculty of the
American University of Sharjah
College of Engineering
In Partial Fulfillment
of the Requirements
for the Degree of

Master of Science in
Mechanical Engineering

Sharjah, United Arab Emirates
May 2021

Declaration of Authorship

I declare that this thesis is my own work and, to the best of my knowledge and belief, it does not contain material published or written by a third party, except where permission has been obtained and/or appropriately cited through full and accurate referencing.

Signed..... *Ahmad Alsaghir*

Date..... 05/26/2021

The Author controls copyright for this report.

Material should not be reused without the consent of the author. Due acknowledgement should be made where appropriate.

© Year 2021

AHMAD MOHAMMAD ALSAGHIR

ALL RIGHTS RESERVE

Approval Signatures

We, the undersigned, approve the Master's Thesis of Ahmad Mohammad Al Saghir

Thesis Title: Computational Fluid Dynamics of Energy Separation in Vortex Tube

Date of Defense: 04/28/2021

Name, Title and Affiliation	Signature
-----------------------------	-----------

Dr. Mehmet Orhan Associate Professor, Department of Mechanical Engineering Thesis Advisor	
---	--

Dr. Mohammad Hamdan Professor, Department of Mechanical Engineering Thesis Co-Advisor	
---	--

Dr. Bassam Abu-Nabah Associate Professor, Department of Mechanical Engineering Thesis Committee Member	
--	--

Dr. Serter Atabay Associate Professor, Department of Civil Engineering Thesis Committee Member	
--	--

Dr. Mamoun Abdel-Hafez Head Department of Mechanical Engineering	
--	--

Dr. Lotfi Romdhane Associate Dean for Graduate Studies and Research College of Engineering	
--	--

Dr. Sameer Al-Asheh Interim Dean College of Engineering	
---	--

Dr. Mohamed El-Tarhuni Vice Provost for Graduate Studies Office of Graduate Studies	
---	--

Acknowledgement

I would like to thank my professors Dr. Mohammad Hamdan and Dr. Mehmet Orhan for their unwavering support and help throughout the journey of this study. Thank you for the fruitful collaboration that instilled in me the researcher mindset and enabled me with a substantial multidisciplinary research experience which I am very proud of.

To all professors who taught me the master courses at AUS, I extend my sincere thanks and great gratitude for their continuous efforts, and guidance till the completion of this stage. I really appreciate your dignified advice and motivation. Moreover, I would like to thank the American university of Sharjah for the generous financial support that is offered as a Graduate Assistantship.

Finally, I am warmly thankful to my family who have supported and motivated me to do the best. Special thanks from the bottom of my heart to my parent who have been the torch that rekindled the way towards my dreams.

Abstract

Devil's Tube is the name that some researchers chose for Ranque-Hilsch vortex tube because of the ambiguity of its working mechanism. In an attempt to unveil the principle of energy separations in this tube, this study uses the shear stress transport $k - \omega$ turbulence model with viscous heating to investigate the flow structure inside the fluid domain and to examine the impact of the fluid's properties on the performance of the temperature separation. Firstly, the flow parameters such as velocity, temperature, pressure, and density are plotted at various locations inside the tube. Thereafter, the energy separation performance is tested using five different gases, namely helium, air, oxygen, nitrogen, and carbon dioxide. In this regard, the effect of the gas properties, such as molecular weight, heat capacity, thermal conductivity, and dynamic viscosity are also examined. The study shows that the minimum cold temperature and the maximum hot temperature are achieved at different mass fractions and that the flow inside Ranque-Hilsch vortex tube consists of a forced vortex from $r/R=0$ to 0.9 and a free vortex from $r/R=0.9$ to 1. Furthermore, a comparison analysis is carried out to observe that helium yields the maximum separation while carbon dioxide yields the lowest; besides, one must account for viscous dissipation in modelling the energy separation in vortex tube. Moreover, energy separation performance improves with lower molecular weight and heat capacity, and higher dynamic viscosity of the working fluids, while no impact of the thermal conductivity is observed. Finally, it is concluded that the energy separation in vortex tube is due to the density gradient along the radial direction.

Keywords: *Vortex Tube; Vortex Flow structure; Energy separation, Viscous heating.*

Table of Contents

Abstract	5
List of Figures	8
List of Tables	10
List of Abbreviations	11
Nomenclature	12
Chapter 1. Introduction	13
1.1. Overview	13
1.2. Thesis Objectives	14
1.3. Research Contribution.....	14
1.4. Thesis Organization	14
Chapter 2. Background and Literature Review.....	15
2.1. Proposed Working Mechanisms	15
2.2. Experimental Studies	16
2.3. Numerical Studies (CFD).....	17
Chapter 3. Methodology	20
3.1. Problem Formulation	20
3.2. CAD Model.....	20
3.3. Preparation of the Numerical Modelling	21
3.4. Extracting results.....	21
Chapter 4. Numerical Setup.....	22
4.1. Computational Domain	22
4.2. Governing Equations.....	23
4.3. <i>SST k – ω</i> turbulence model	24
4.4. Physical Setup and Boundary Conditions	25
4.5. Mesh Independence.....	25
Chapter 5. Results and Analysis	27
5.1. Testing Different Gases	27
5.2. Flow Structure.....	29
5.2.1. Velocity.....	29
5.2.2. Pressure	31
5.2.3. Temperature.....	32
5.3. Effect of Molecular Weight	34

5.4.	Effect of Thermal Conductivity	40
5.5.	Effect of Heat Capacity	41
5.6.	Effect of Dynamic Viscosity	45
5.7.	Effect of Tube Diameter	51
5.8.	Effect of Tube Length	53
Chapter 6. Conclusion and Future Work		61
References		63
Vita		66

List of Figures

Figure 1: Circulation inside vortex tube.	16
Figure 2: 3D CAD model.....	20
Figure 3: A three-dimensional model of the vortex tube in 90° sector.....	22
Figure 4: A two-dimensional schematic of the vortex tube with its main dimensions.....	23
Figure 5: Unstructured mesh of the modeled vortex tube with its inflation layer.	26
Figure 6: Effect of number of elements on the hot outlet temperature.....	26
Figure 7: Validating the SST $k-\omega$ turbulence numerical simulation with the experimental data in [16] by plotting outlet temperature ratio at different mass fraction.	28
Figure 8: Mach number contour at the periodic surface.	28
Figure 9: Effect of cold mass fraction on the dimensionless total outlet temperature for different gases.....	29
Figure 10: Velocity profiles inside the vortex tube at different locations (a) tangential magnitude (b) axial velocity (c) total velocity.	31
Figure 11: Velocity streamlines at the periodic surface.....	31
Figure 12: Pressure profiles inside the vortex tube at different locations (a) static pressure (b) total pressure.	33
Figure 13: Density profile inside the vortex tube at different locations.	34
Figure 14: Temperature profiles inside the vortex tube at different locations (a) static temperature (b) total temperature.....	35
Figure 15: Effect of molecular weight ratios on dimensionless (a) Static and (b) Total outlet temperatures.....	36
Figure 16: Dimensionless velocity profiles versus dimensionless radial direction plotted at $z/L=0.63$ for various molecular weight ratios.....	37
Figure 17: Dimensionless pressure profiles versus radial direction plotted at $z/L=0.63$ for various molecular weight ratios. (a) Static and (b) Total pressures.....	38
Figure 18: Dimensionless density profiles versus dimensionless radial direction plotted at $z/L=0.63$ for various molecular weight ratios.....	39
Figure 19: Dimensionless temperature profiles versus dimensionless radial direction plotted at $z/L=0.63$ for various molecular weight ratios. (a) Static and (b) Total temperatures.....	40
Figure 20: Dimensionless static temperature profiles versus dimensionless radial direction plotted at $z/L=0.63$ for various thermal conductivity ratios.	41
Figure 21: Effect of heat capacity ratios on dimensionless (a) Static and (b) Total outlet temperatures.....	43
Figure 22: Dimensionless velocity profiles versus dimensionless radial direction plotted at $z/L=0.63$ for various heat capacity ratios.....	44
Figure 23: Dimensionless pressure profiles versus dimensionless radial direction plotted at $z/L=0.63$ for various heat capacity ratios. (a) Static and (b) Total pressures. .	45
Figure 24: Dimensionless temperature profiles versus dimensionless radial direction plotted at $z/L=0.63$ for various heat capacity ratios. (a) Static and (b) Total temperatures.....	47
Figure 25: Effect of dynamic viscosity ratios on dimensionless (a) Static (b) Total outlet temperatures.	48

Figure 26: Dimensionless velocity profiles versus dimensionless radial direction plotted at $z/L=0.63$ for various viscosity ratios.	48
Figure 27: Dimensionless pressure profiles versus dimensionless radial direction plotted at $z/L=0.63$ for various dynamic viscosity ratios. (a) Static and (b) Total pressures.	49
Figure 28: Dimensionless density profiles versus dimensionless radial direction plotted at $z/L=0.63$ for various dynamic viscosity ratios.	50
Figure 29: Dimensionless temperature profiles versus dimensionless radial direction plotted at $z/L=0.63$ for various dynamic viscosity ratios. (a) Static and (b) Total temperatures.	51
Figure 30: Variation of heating capacity with tube diameter.	52
Figure 31: Effect of diameter ratio on hot outlet temperature.	53
Figure 32: Effect of diameter ratio on the density values inside the flow domain.	54
Figure 33: Effect of diameter ratio on cold temperature.	54
Figure 34: Effect of diameter ratio on the mass flow rate.	55
Figure 35: Variation of cooling capacity with tube diameter.	56
Figure 36: Effect of diameter ratio on cold temperature.	56
Figure 37: Effect of tube length on cooling capacity.	57
Figure 38: Effect of length ratio on heating capacity.	57
Figure 39: Effect of length ratio on hot outlet temperature.	57
Figure 40: Effect of length ratio on mass flow rate.	58
Figure 41: Effect of length ratio on static temperature.	58
Figure 42: Effect of tube length on cooling capacity.	59
Figure 43: Effect of tube length on cold total temperature.	59
Figure 44: Demonstration of isentropic compression phenomenon.	60

List of Tables

Table 1: Dimensions of the vortex tube.....	22
Table 2: Thermo-Physical properties of the tested gases.....	27
Table 3: Effect of thermal conductivity on outlet temperatures.	41

List of Abbreviations

<i>COP</i>	Coefficient of performance
<i>DV</i>	Dynamic Viscosity
<i>HC</i>	Heat Capacity
<i>MW</i>	Molecular Weight
<i>RHVT</i>	Ranque-Hilsch vortex tube
<i>TC</i>	Thermal Conductivity
<i>VT</i>	Vortex tube

Nomenclature

List of symbols

D_ω	Cross diffusion term
\bar{G}_k	Generation of k
G_ω	Generation of ω
K	Thermal conductivity
k	Turbulent kinetic energy
P_{atm}	Atmospheric pressure
P_{in}	Inlet pressure
Pr	Prandtle number
R_t	Radius of the tube
R	Gas constant
S_k	User define source term of k
S_ω	User define source term of ω
T	Temperature
T_{in}	Inlet temperature
T_s	Static temperature
T_t	Total temperature
V	Velocity
V_{in}	Inlet velocity
Y_k	Dissipation of k
Y_ω	Dissipations of ω

Greek Symbols

Γ_k	Effective diffusivity of k
Γ_ω	Effective diffusivity of ω
Δ	Change in value
μ	Dynamics viscosity
ρ	Density
φ	Viscous heat generation
ω	Specific dissipation

Chapter 1. Introduction

In this chapter, we provide a short introduction about the vortex tube and its controversial proposed working mechanisms. Then, we present the objective of this study as well as the thesis contribution. Finally, general organization of the thesis is presented.

1.1. Overview

A vortex tube (VT) is a thermo-fluidic device that is capable of splitting a pressurized fluid into hot and cold currents simultaneously, without any moving parts or chemical reactions. It was accidentally discovered by a French scientist in 1933 [1]. In 1947, a German scientist modified the structural parameters of the tube to improve its performance [2]. VT consists of inlet nozzles where fluid is admitted in a tangential manner (known as vortex generator), a strait tube, a cold orifice, and a hot orifice with a control valve to adjust the mass flow fractions. VT has a wide range of spot cooling applications. For instance, it is used for cooling milling machining to preserve the properties of the work piece and protect the cutting tools [3, 4], cooling the working suits of mines workers [5], solid–liquid separators [6], convex mirror cooling [7] or other air-conditioning systems [8]. The feasibility of using a vortex tube in water desalination is also reported by [9].

Currently, there is no consensus on how the energy separation effect in VT take place. Nonetheless, many theories have been proposed to explain this phenomenon [10-12]. For instance, the viscous shear theory suggests that the angular velocity increases towards the center and tends to conserve the angular momentum of the fluid, which in turn transfers the excess kinetic energy to the periphery of the tube through the shear force [10, 11]. Another theory has proposed [12] that the cause of temperature difference is a phenomenon named “acoustic streaming”. This phenomenon relates the acoustics waves generated at the hot outlet to the formation of some secondary flows and turbulent eddies inside the tube.

Hilsh’s modifications [2] and the advantages of VT have motivated the scientific community to look for further ways to improve its operating efficiency. Many experimental and numerical studies have been carried out to investigate the effect of the structural parameters as well as the operating conditions on the performance of the vortex tube.

1.2. Thesis Objectives

To help the ongoing efforts, the objective of this study is to numerically investigate the flow structure inside a vortex tube, such as the radial distribution of velocity, pressure, and temperature at different locations. Moreover, it aims at investigating the effect of fluid viscosity on temperature separation in Ranque-Hilsch vortex tube; besides, presenting a detailed examination of various working fluids and their thermophysical properties such as heat capacity, molecular weight, and thermal conductivity on the radial velocity profile of the gas, temperature, and pressure at specific locations in the tube.

1.3. Research Contribution

The contributions of this research work can be summarized as follows:

- Propose the wall treatment function that can be used to properly predict the flow field and the energy separation inside the tube.
- Examines the impact of fluid properties on the performance of the tube.
- Explain the impact of fluid's viscosity on the phenomenon of temperature separation at the two ends of the tube.
- Proof that the radial density gradient is the main reason of temperature separation inside the tube.

1.4. Thesis Organization

The rest of the thesis is organized as follows: Chapter 2 provides background and literature review about VT where we depict some of the related experimental and numerical research. Moreover, related works to this research are discussed. The employed methods and algorithms are discussed in After that, Chapter 3 presents the methodology that has been followed to come up with the results of this research. along with the implementation of the proposed architecture. Chapter 4 presents the flow structure evaluation and the impact of the thermophysical properties. Finally, Chapter 5 concludes the thesis and outlines the future work.

Chapter 2. Background and Literature Review

Vortex tube is a mechanical device that enables the instantaneous splitting of a room temperature pressurized fluid stream into a low and a high temperature stream. It consists of a group of inlet nozzles mounted tangentially on the wall of a circular tube, a cold outlet at the center of the tube, and a hot outlet equipped with a regulating valve to control the mass fractions. When a fluid is injected through the nozzles, a spinning vortex is generated inside the tube, where part of the fluid leaves through the high temperature outlet and the other part bounce back to leave through the cold temperature outlet. Although Ranque-Hilsch vortex tube (RHVT) has low thermal efficiency, it has a wide range of positive aspects, which make it attractive for many industrial applications. Vortex tube is a durable device since (1) it needs little maintenance as it has no moving parts, (2) it does not need special working fluid (Freon or other refrigerants), (3) it has light weight and (4) its outlet temperatures are easily adjustable.

2.1. Proposed Working Mechanisms

Despite being used in various industrial applications, the working mechanism of vortex tube is still contentious. In 1933, [1] argued that the energy separation is due to the adiabatic expansion in the near axis region and adiabatic compression in the peripheral region. This idea has been adopted by [2] in 1947 who also considered the viscous effect between fluid layers. However, the idea of fully adiabatic process has been later disproved by different research groups [13-15]. Researchers [15] has pointed that the friction between fluid's layers is the main reason of temperature separation. Before fluid flows away from the vortex generator, the structure of the flow consists mainly of a free vortex. In this region friction allows the transfer of the kinetic energy, between the free and the forced vortex, in a higher rate than the transfer of heat. Consequently, the internal energy of the peripheral fluid will be higher than that of the near axis fluid. This argument has been supported by [13] who also states that the turbulent motion that are formed just at the outlet of the inlet nozzles cause mass transfer which in turn leads to the exchange of kinetic and heat energy. [16] has claimed that turbulent mixing and turbulent shear work are the main reasons of the energy separation phenomenon. These proposals cannot be fully accepted because those researchers used various turbulence parameters, which are difficult to be equal in all investigations, and they do not utilize the effect of geometrical parameters [17].

In 1990s, [18-20] proposed the secondary circulation model which refers the origin of energy transfer to the presence of two types of secondary circulation inside the tube, open and closed circulations, Figure 1. The open circulation is named the peripheral loop, and it passes from the outlet of the inlet nozzles towards the hot orifice then bounce back to leave through the cold orifice. This loop can be divided into two portions, high temperature portion at the periphery of the tube and low temperature portion at the center of the tube. The closed circulation is named the secondary circulation loop, and it is enclosed by the peripheral loop. These two loops combined work as a refrigeration cycle where work is transferred from the peripheral to the near axis region and heat is transferred from the near axis region to the peripheral region. In this model, friction between fluid layers plays a crucial role where it decelerates the peripheral fluid adiabatically increasing its temperature [17]. Acoustic streaming is another proposed working mechanism of Ranque-Hilsch vortex tube. It states that the acoustic wave generated by organized disturbances alters the free vortex to forced vortex, which leads to temperature separation [12].

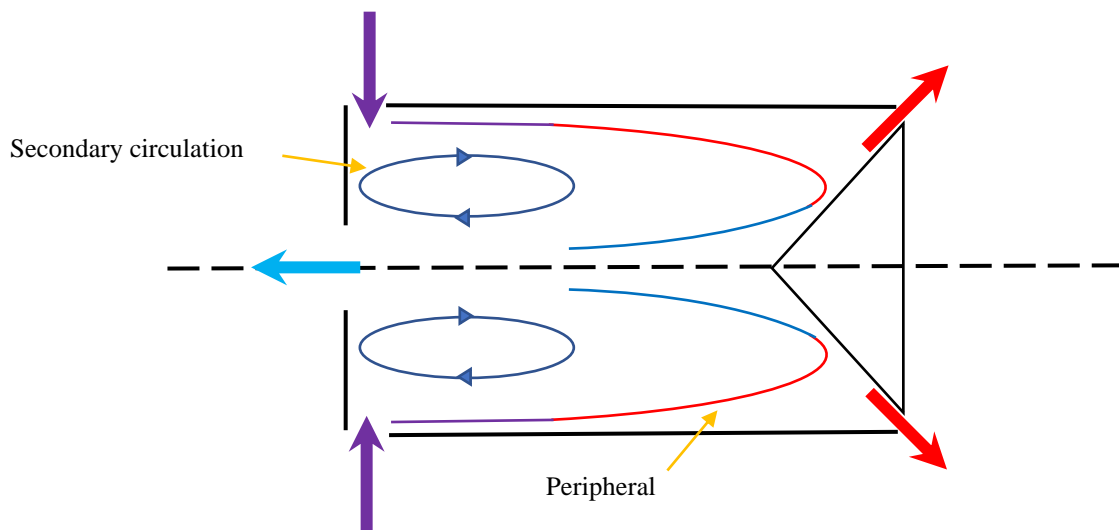


Figure 1: Circulation inside vortex tube.

2.2. Experimental Studies

Many experimental studies have been carried out to investigate the effect of the structural parameters as well as the operating conditions on the performance of the vortex tube. [21] have experimentally investigated the effect of 4 different design parameters, namely (1) inlet pressure, (2) tube length, (3) tube diameter, and (4) tube tapered angle, on

the performance of the vortex tube. It was reported that the inlet pressures rise achieves a greater the temperature difference until a peak value, after which the performance starts to deteriorate [21]. It was suggested that the performance deterioration occurs due to the inlet nozzles choked condition. The effect of tube's roughness has been investigated by [22] and it was reported that the efficiency of VT decreases as the tube's roughness increases. A group of researchers [23] investigated the effect of number of inlet nozzles on the temperature separation. The measurements showed that the energy separation increases with more nozzles and this improvement has been referred to the increase in the swirl intensity. Similar results have been reported by [24] who have stated that the efficiency of the vortex tube with 4 and 6 inlet nozzles are better than with 2 inlet nozzles.

Beside the number of nozzles, their size also has a great effect on the separation. [25] have revealed that a smaller nozzle area results in a higher separation magnitude. Also, [26] have investigated the effect of nozzle to tube's diameter ratio. The results showed the highest cold temperature difference at an optimum diameter ratio of 0.64. Another study [27] has presented that increasing the number of inlet jets leads to hotter and colder currents at the outlets, which does not necessary leads to a rise in the heating and cooling load of the VT. It has also been reported that the minimum and the maximum temperatures do not occur at the same mass fractions.

Working fluid is another crucial parameter in the separation. [28] has tested oxygen as a working fluid and the measurements showed that it gives higher temperature difference than air. After testing various type of refrigerants, [29] have achieved the highest temperature difference by using R728. [30] have tested the performance of serial and parallel connected RHVT, using carbon dioxide (CO₂) as a working fluid. They have reported that the efficiency of the parallel connection is higher than that of serial connection, and using CO₂ gives relatively lower temperature difference than oxygen and air.

2.3. Numerical Studies (CFD)

Employing their ability to provide details of flow structure under different operating conditions, many scientists have used numerical simulation to better understand the flow structure inside the VT. For instance, [31] have used 2D axisymmetric model to

numerically investigate the energy separation in a VT. It was reported that the magnitude of radial velocity component was very small compared to the axial and swirl velocities. Also, the static temperature decreased in the radial direction, which led to heat transfer in the radial direction. The SST $k - \omega$ turbulence model is used by [32] to examine the flow field inside vortex tube. It was found that the flow domain mainly consists of a forced vortex and that expansion is the only cooling mechanism in vortex tube. [33] has used ANSYS fluent package to study VT flow and has tested two numerical turbulence models, namely, standard $k-\varepsilon$ and RNG $k-\varepsilon$. By comparing the numerical models with the experimental measurements, it has been observed that both models under predict the outlet's temperatures, the standard $k-\varepsilon$ results being closer to the experimental values. Another group of researchers [34] have investigated the impact of the adiabatic walls assumption on the outlets temperature difference. It was found that at small cold mass fraction, this assumption has a mild influence compared to that at high mass fraction.

A 3D numerical model is used by [35] to investigate the effect of number of inlet jets on the streamlines. It has been concluded that the streamlines followed a similar pattern as in axisymmetric assumption only in case of large number of nozzles. Different turbulence models, namely standards $k-\varepsilon$, standard $k-\omega$, SST $k-\omega$, and RSM, have been tested by [36]. Then, the outcomes have been compared with published experimental data [37]. The researchers have found that all of the turbulence models are able to predict the energy separation phenomenon. However, only the RSM model was in agreement with the experimental temperature difference. These findings match the outcomes of [38] who compares the results of RNG $k - \varepsilon$, and RSM RANS models with that of LES model.

Using computational fluid dynamics (CFD) simulation, [39] have reported that a secondary flow structure may cause deterioration in the VT performance. Another numerical investigation [40], using standards $k-\varepsilon$, RNG $k-\varepsilon$, standard $k-\omega$, and SST $k-\omega$, has showed that all models are in good agreement with the experimental work, except the RNG $k-\varepsilon$ model. This result contradicts with [30] that has numerically investigated the energy separation in vortex tube using $k-\varepsilon$ and RNG $k-\varepsilon$, and reported that the RNG $k-\varepsilon$ provided a better energy separation prediction. Researchers [41] have investigated the energy separation of VT using different turbulence models. Their results have pointed out

that the Spalart-Allmaras model over predicted the cold and hot temperature, while the RSM under predicted these temperatures.

The effect of tube diameter and tube length on the performance of the VT was tested by [42]. It was claimed that the best performance was obtained at a length to diameter ratio of 9.3. Furthermore, the study has reported that the temperature difference between the cold and the hot outlets increases with the length of the tube. [43] have numerically studied the effect of both the numerical scheme (hybrid, upwind, and second order upwind) and the turbulence models (k - ϵ and algebraic stress model (ASM) models) on the calculation of energy separation in a parallel flow vortex tube. They have reported that the three numerical schemes have no effect on the prediction of the temperature difference. Moreover, [44] have utilized the LES model to examine the energy separation in axisymmetric VT model. The results have stated that the minimum total temperature occurred near the tube center, while the maximum temperature near the tube periphery. Furthermore, it was indicated that the minimum value of static and total temperatures were close to each other. Add to this [44] have reported that the difference between static and total temperatures at the periphery of the tube was due to the conversion of kinetic energy into thermal energy. In this regard, another numerical study [45] has used standard k - ϵ turbulence model and showed a good agreement with experimental results.

Chapter 3. Methodology

3.1. Problem Formulation

In consideration of the proposed working mechanisms, friction between fluid layers seems of great significance in energy separation phenomenon. Moreover, the studies that have been done on the effect of the working fluid do not show the impact of the individual fluid property, although they refer the improvement or deterioration of performance to the values of the molecular weight and heat capacity. Therefore, for the first time, this novel study investigates the effect of fluid viscosity on temperature separation in Ranque-Hilsch vortex tube and presents a detailed examination of the effect of various fluids and fluid properties such as heat capacity, molecular weight, and thermal conductivity on the radial velocity profile of the gas, temperature and pressure at specific locations in the tube. Moreover, it offers an insight investigation of the flow structure in vortex tube.

3.2. CAD Model

Figure 2 shows a 3D model of a commercialized vortex tube whose dimensions are obtained from literature [46]. This model is generated using ANSYS DesignModeler. The inlet nozzle is mounted tangentially on the main tube to mimic the vortex generator in the actual model.

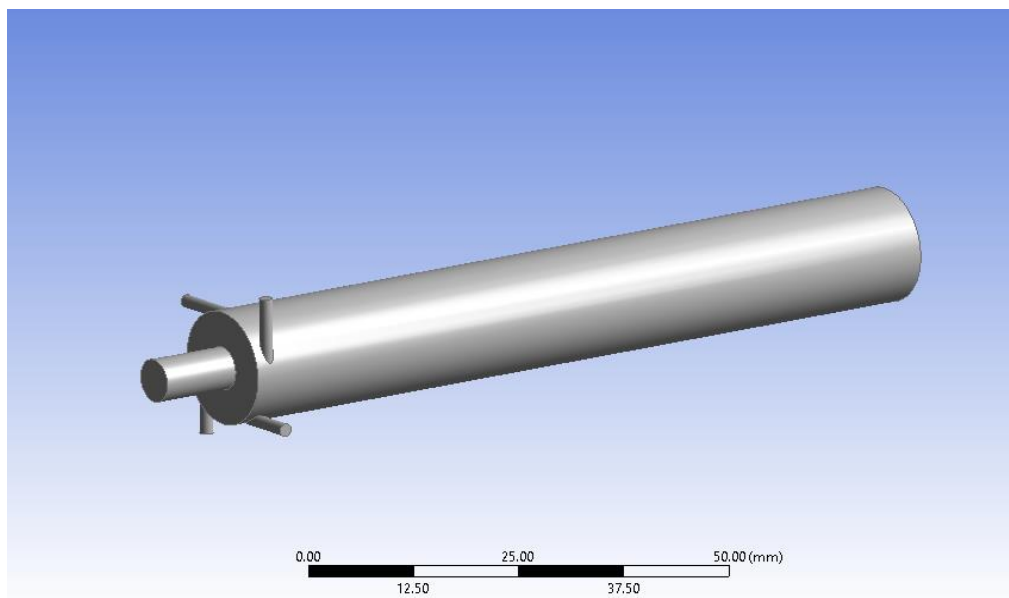


Figure 2: 3D CAD model.

3.3. Preparation of the Numerical Modelling

The numerical model is generated using a commercial finite volume CFD software, ANSYS-fluent. Steady, pressure-based solver is utilized to simulate the energy separation phenomenon in a VT. In the solution method the coupled scheme is used with third order discretization in density, momentum, energy, turbulent kinetic energy, and specific dissipation rate equations. Air is chosen to be the control gas, and its default properties are used to non-dimensionalize the independent variable properties. The residuals are set to 10^{-9} for energy and to 10^{-6} for continuity, velocity, k , and ω .

3.4. Extracting results

In order to make sure that the outcomes of this study is reliable and robust, the impact of cold mass fraction on the outlet's temperature are compared with the experimental findings of [46]. The cold mass fraction is changed by adjusting the hot outlet pressure instead of changing its area. After that, the flow parameters at 15mm, 30mm, 45mm, 60mm, 75mm, 85mm, are extracted and plotted using Microsoft Excel. These parameters are nondimensionalized based in the inlet boundary conditions.

Chapter 4. Numerical Setup

4.1. Computational Domain

A schematic of the three-dimensional VT is shown in Figure 3. The dimensions of the vortex tube used in this study are obtained from an earlier experimental study [46]. To reduce the computational time, a quarter of the model is simulated with a periodic rotational boundary condition. The vortex generator is replaced by inlet jets mounted tangentially on the main tube. The dimensions used in the analysis are listed in Table 1 and are illustrated in Figure 4. To simplify the generation of structured mesh, the 3D model is divided into three subdomains. The numerical model is generated using a commercial finite volume CFD software, ANSYS-fluent.

Table 1: Dimensions of the vortex tube.

Parameter	Dimension (mm)
Tube radius (R_t)	7.24
Tube length (L_t)	97
Cold outlet length (L_c)	10
Cold outlet radius (r_c)	2.715
Nozzle diameter (d)	1.6
Inlet pipe (D)	16

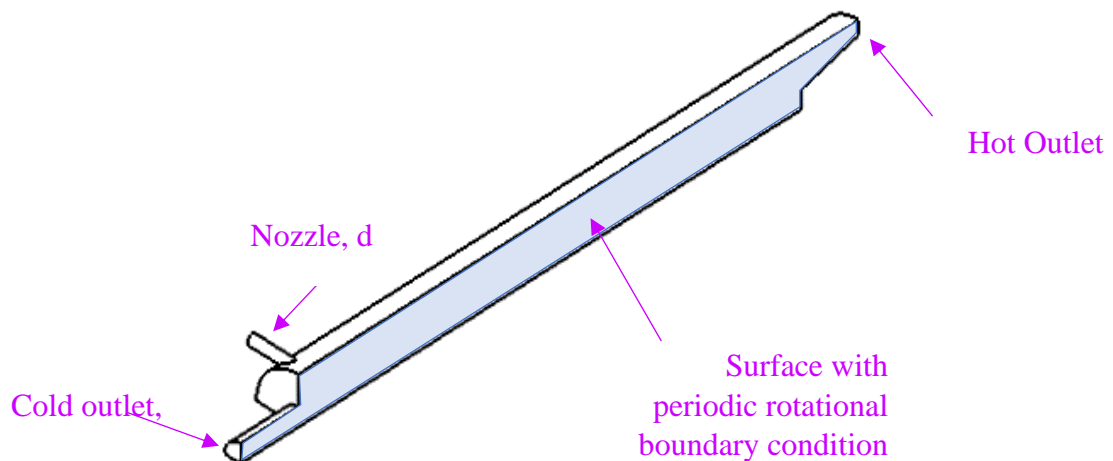


Figure 3: A three-dimensional model of the vortex tube in 90° sector.

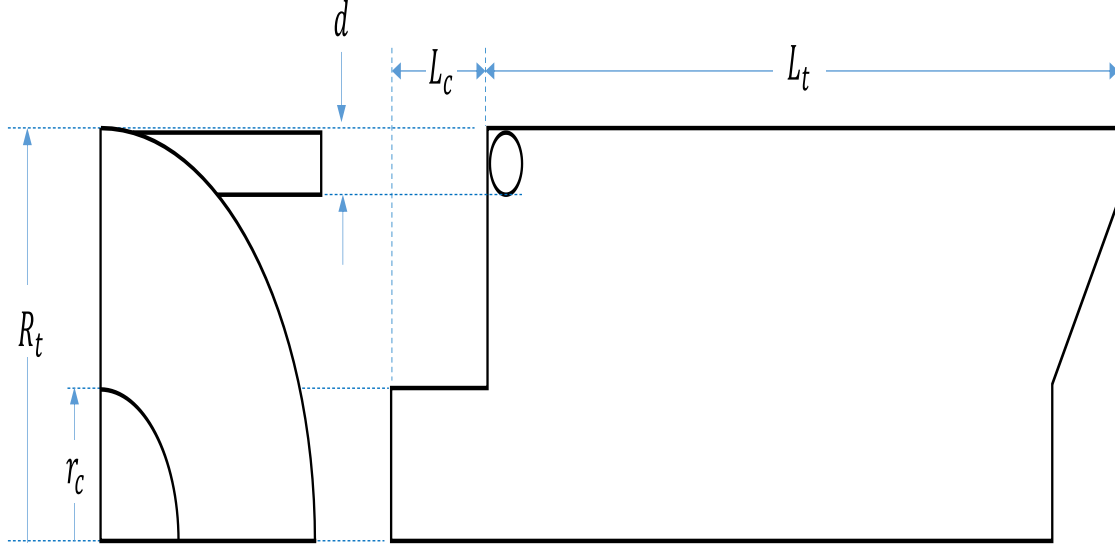


Figure 4: A two-dimensional schematic of the vortex tube with its main dimensions.

4.2. Governing Equations

In order to obtain flow structure and temperature of air flow in a vortex tube, one need to simultaneously solve the conservation equations with the ideal gas equation.

Conservation of mass:

$$\frac{\partial(\rho\bar{u}_i)}{\partial x_j} = 0 \quad (1)$$

Conservation of momentum:

$$\frac{\partial(\rho\bar{u}_i\bar{u}_j)}{\partial x_j} = -\frac{\partial\bar{p}}{\partial x_i} + \frac{\partial}{\partial x_j} \left[\mu \left(\frac{\partial\bar{u}_i}{\partial x_j} + \frac{\partial\bar{u}_j}{\partial x_i} \right) - \rho\overline{u'_i u'_j} \right] \quad (2)$$

Conservation of energy:

$$\frac{\partial(\rho\bar{u}_j\bar{T})}{\partial x_j} = \frac{\partial}{\partial x_j} \left[\frac{\mu}{Pr} \left(\frac{\partial\bar{T}}{\partial x_j} \right) - \rho\overline{T' u'_j} \right] + \varphi \quad (3)$$

Ideal gas law:

$$\bar{p} = \rho R \bar{T} = \rho (R_u / MW) \bar{T} \quad (4)$$

where, \bar{u} , \bar{T} , and \bar{p} are the time-average velocity, temperature, and pressure, respectively. u'_j and T' are the instantaneous fluctuating velocity and temperature. Reynold's tensors in equations 2 and 3 are modelled using Boussinesq approach as per the following equations (Eqs. 5-6):

$$\overline{\rho \dot{u}_i \dot{u}_j} = \mu_t \left(\frac{\partial u_i}{\partial x_j} + \frac{\partial u_j}{\partial x_i} \right) - \frac{2}{3} \left(\rho k \delta_{ij} + \mu_t \frac{\partial u_k}{\partial x_k} \right) \quad (5)$$

$$\overline{\rho \dot{T}_i \dot{u}_j} = - \frac{\mu_t}{Pr_t} \left(\frac{\partial T}{\partial x_j} \right) \quad (6)$$

where, μ_t , k and Pr_t are the turbulent viscosity, turbulent kinetic energy, and turbulent Prandtl number, respectively. The merit of this approach is the low computational cost associated with the calculation of μ_t . In this study the turbulent viscosity is computed in terms of the turbulent kinetic energy (k) and the specific dissipation rate (ω).

4.3. SST $k - \omega$ turbulence model

The SST $K - \omega$ turbulence model is used to model the turbulence flow. The SST $K - \omega$ turbulence model is a two-equation model where the turbulent viscosity is computed by utilizing the turbulent kinetic energy (k) and the specific dissipation rate (ω) as shown in the following equation:

$$\mu_t = \alpha^* \frac{\rho k}{\omega} \quad (7)$$

where, α^* is a correction number used to damp the turbulent viscosity at low Reynold number. k and ω can be calculated using the following equations[47]:

$$\frac{\partial}{\partial t}(\rho k) + \frac{\partial}{\partial x_i}(\rho k u_i) = \frac{\partial}{\partial x_i} \left(\Gamma_k \frac{\partial k}{\partial x_j} \right) + \bar{G}_k - Y_k + S_k \quad (8)$$

$$\frac{\partial}{\partial t}(\rho \omega) + \frac{\partial}{\partial x_i}(\rho \omega u_i) = \frac{\partial}{\partial x_j} \left(\Gamma_\omega \frac{\partial \omega}{\partial x_j} \right) + G_\omega - Y_\omega + D_\omega + S_\omega \quad (9)$$

More detail regarding the variables shown in equations (8) and (9) are explained in ANSYS user guide [47].

The equations above are solved numerically under the assumption of steady state where thermal conductivity, heat capacity and dynamic viscosity are assumed constant. This assumption is acceptable since the expected temperature change is less than 35°C. This assumption is adopted to allow studying the effect of varying these properties with large difference. The viscous dissipation is examined in this study, since Brinkman number (Br) is of order 1, where $r = \mu V^2 / (k \Delta T)$.

4.4. Physical Setup and Boundary Conditions

Steady, pressure-based solver is utilized to simulate the energy separation phenomenon in a VT. In the solution method the coupled scheme is used with third order discretization in density, momentum, energy, turbulent kinetic energy, and specific dissipation rate equations. Five different gases, namely, air, oxygen, nitrogen, carbon dioxide and helium are examined. Table 2 shows the default properties of these gases that are provided by ANSYS CFD tool. Air is chosen to be the control gas, and its default properties are used to non-dimensionalize the independent variable properties. The residuals are set to 10^{-9} for energy and to 10^{-6} for continuity, velocity, k , and ω . The physical boundary conditions that are used in this study are as follow:

- a. Rotational periodic boundary conditions about the axis of the tube.
- b. A 4-bar pressure inlet boundary condition.
- c. A 0.3 bar pressure outlet boundary condition at the hot end.
- d. A 0-bar pressure outlet boundary condition at the cold end.
- e. An adiabatic with no slip boundary condition at the walls of the tube.

4.5. Mesh Independence

Figure 5 shows the unstructured mesh that is used in this research. A first inflation layer thickness of 1mm and 1.2 growth rate are applied at the tube walls to properly capture the viscose sublayer (by maintaining a y^+ near the wall less than 5). To make sure that the obtained results are independent of number of nodes within the grid, a mesh independent study is done based on the observation of the hot outlet temperature as shown in Figure 6. It is clear that at 720,175 elements, which corresponds to 0.4 mm element size, the effect of element size becomes trivial, which indicates that the mesh independence is achieved at this size.

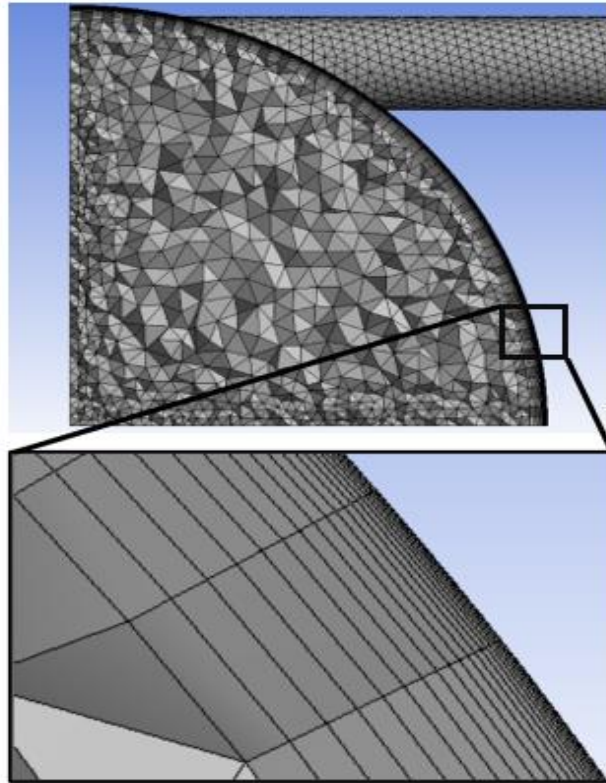


Figure 5: Unstructured mesh of the modeled vortex tube with its inflation layer.

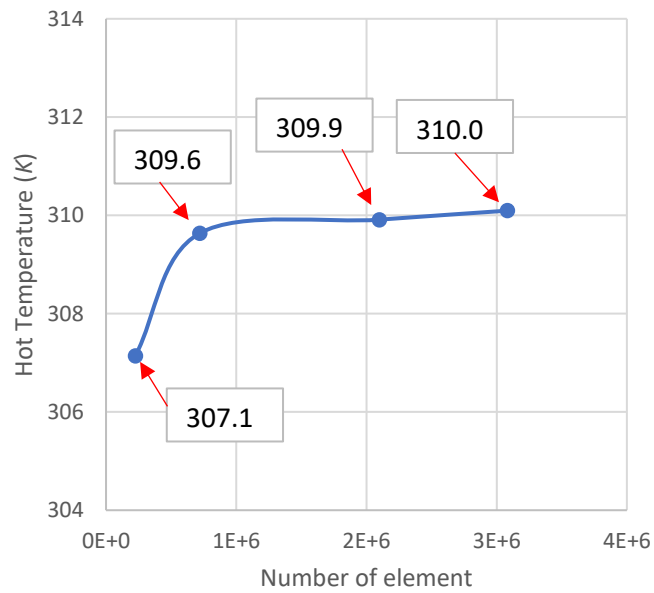


Figure 6: Effect of number of elements on the hot outlet temperature.

Chapter 5. Results and Analysis

Dimensionless parameters are used to demonstrate the results of the numerical simulation. $P_{in} = 4 \text{ bar}$, $T_{in} = 300 \text{ K}$ and the inlet velocity of air are used to produce the dimensionless parameters. All profiles are obtained at dimensionless z-axis distance of $z/L = 0.63$. Regarding the physical properties, they are nondimensionalized based on the values of air properties provided in Table 2. The numerical results are validated by reproducing the experimental work [46] as shown in Figure 7. From this figure, an acceptable agreement is found between *SST* $k - \omega$ model and the experimental results, however, when viscous heating is enabled, this model over predict the experimental findings as a result of ignoring the effect of heat dissipation at the surface of the tube. It is worth emphasizing that the viscous dissipation phenomenon mainly acts in the vortex generator region because this is the only region where Mach number exceeds 1, as shown in Figure 8. Hence, viscous dissipation is adopted for the rest of the study.

Table 2: Thermo-Physical properties of the tested gases.

Gas	Molecular Weigh [$kg/kmol$]	Heat Capacity [$J/kg.K$]	Dynamic Viscosity [$kg/m.s$]	Thermal Conductivity [$W/m.K$]	Gas Constant [J/ $Kg.K$]
Air	28.966	1006.43	1.7894e-05	0.0242	287
Oxygen	31.9988	919.31	1.919e-05	0.0246	260
Nitrogen	28.0134	1040.67	1.663e-05	0.0242	297
Helium	4.0026	5193	1.99e-05	0.152	208
Carbon dioxide	44.00995	840.37	1.37e-05	0.0145	189

5.1. Testing Different Gases

Figure 9 depicts the influence of the cold mass fraction on the energy separation in a vortex tube operating with different gases. As it was shown experimentally for air [46], the relationship between the temperature of the outlets and the mass fractions is non monotonic, and the optimum hot and cold temperatures occur at different mass fractions.

Moreover, it is clear that the best temperature separation is achieved by helium, which has the highest heat capacity (HC) and the lowest molecular weight (MW). On the other hand, carbon dioxide with the lowest HC and the highest MW yields the lowest energy separation performance, which agree with published numerical results [48]. When the vortex tube is modelled with air, nitrogen, or oxygen, the simulations show that these gases behave in a similar way and no significant difference in outlet temperature has been observed. One can attribute this to the fact that these gases have similar HC and MW.

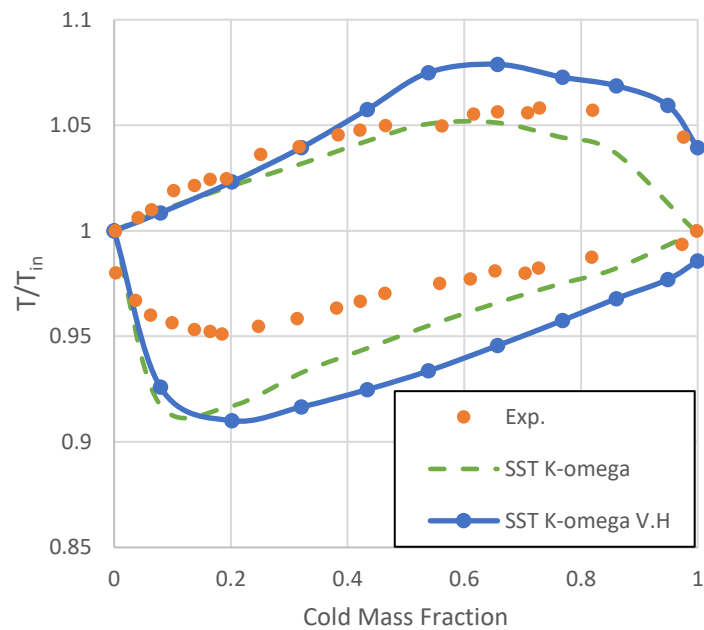


Figure 7: Validating the SST $k-\omega$ turbulence numerical simulation with the experimental data in [16] by plotting outlet temperature ratio at different mass fraction.

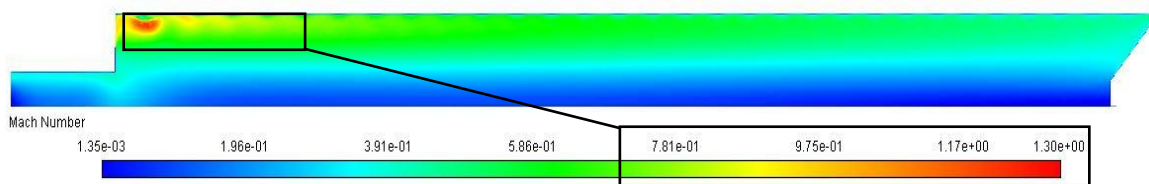


Figure 8: Mach number contour at the periodic surface.

Figure 9 results show that the performance of energy separation depends on many properties such as molecular weight, thermal conductivity, heat capacity and dynamics viscosity. In order to properly investigate the impact of each property, a numerical

simulation is performed varying only one property while fixing the rest of the properties as show in next sections.

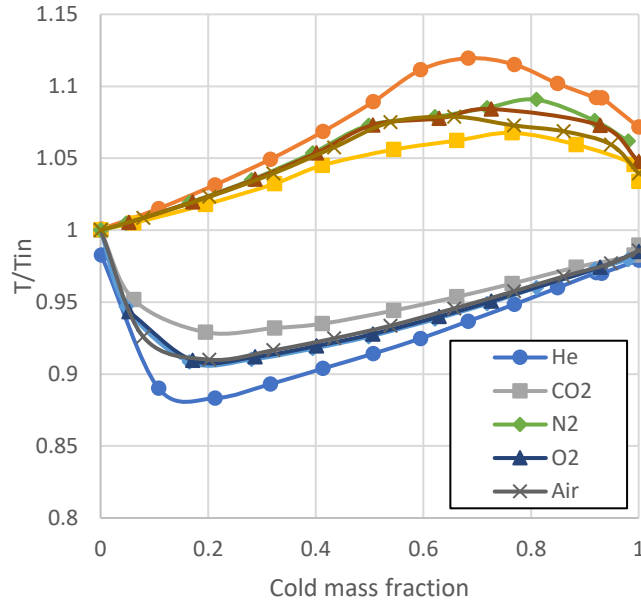
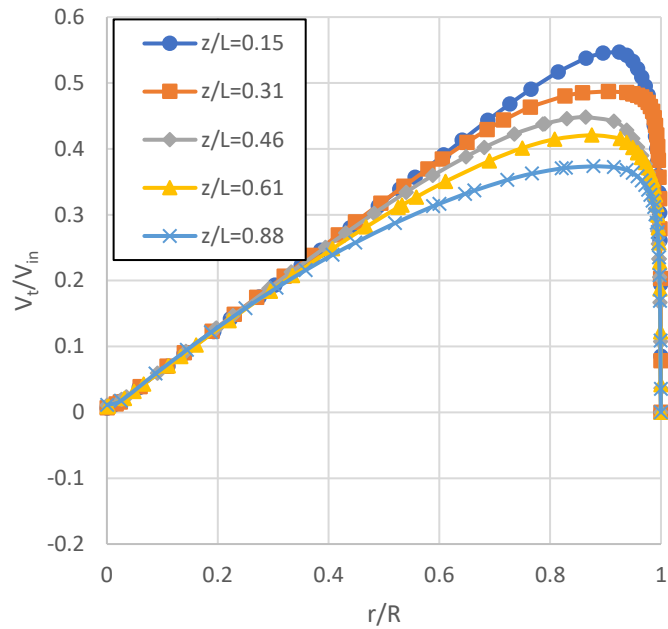


Figure 9: Effect of cold mass fraction on the dimensionless total outlet temperature for different gases.

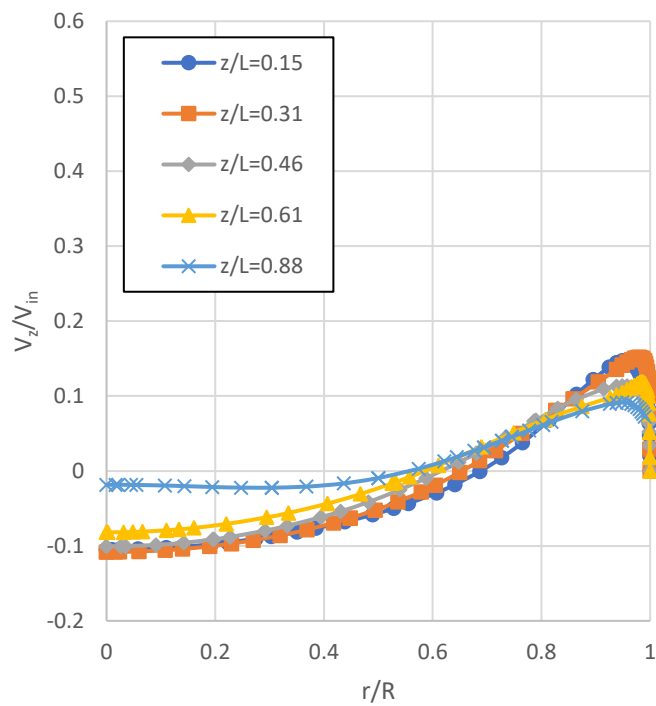
5.2. Flow Structure

5.2.1. Velocity. Figure 10 (a) shows the tangential fluid velocity that varies with radius direction at different axial locations along the VT. This trend reveals the fact that the flow structure inside the vortex tube consists of a forced vortex (Rankin vortex) and free vortex. In the forced vortex region ($\frac{r}{R}$ from 0 to 0.9), the fluid velocity increases linearly with radius, while in the free vortex region ($\frac{r}{R}$ from 0.9 to 1.0), the fluid velocity decreases nonlinearly with radius and reaches to zero at the wall surfaces. Moreover, as seen from the figure, the fluid velocity at the center decreases as the fluid moves towards the hot end and approaches to zero just before the hot valve, at $z/L=0.88$. Figure 10 (b) and (c) shows the axial and tangential velocities, respectively. In Figure 10 (b), the inner region of the VT moves toward the cold outlet, while the fluid near the wall moves toward the hot outlet. The diameter of this inner region decrease as fluid moves towards the hot end. For example, at $z/L=0.15$ the radius ratio is 0.65, while at $z/L=0.46$ the radius ratio is about 0.5. At $z/L=0.15$, majority of fluid with a negative axial velocity either leave through the cold outlet or split into two portions. This motion is clearly visible in Figure 11, where the fluid domain divides into three parts. The first portion circulates in the vortex generator region,

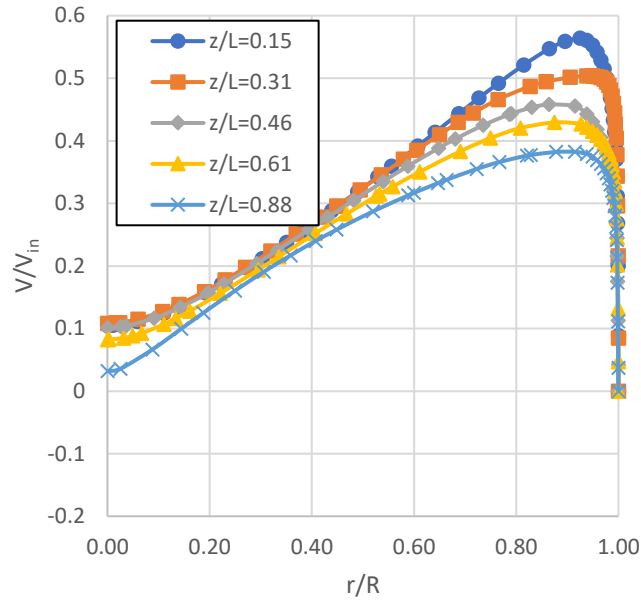
the second part leaves through the cold end, and the third one leaves through the hot end. In the peripheral region the axial velocity magnitude decreases along the tube length, while increases in the central region. This trend is due to the momentum transfer from the outer (no slip condition at the wall surface) to the core region.



(a)



(b)



(c)

Figure 10: Velocity profiles inside the vortex tube at different locations (a) tangential magnitude (b) axial velocity (c) total velocity.

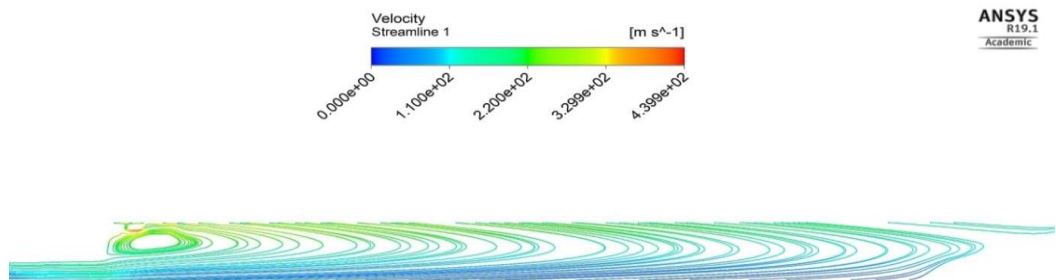


Figure 11: Velocity streamlines at the periodic surface.

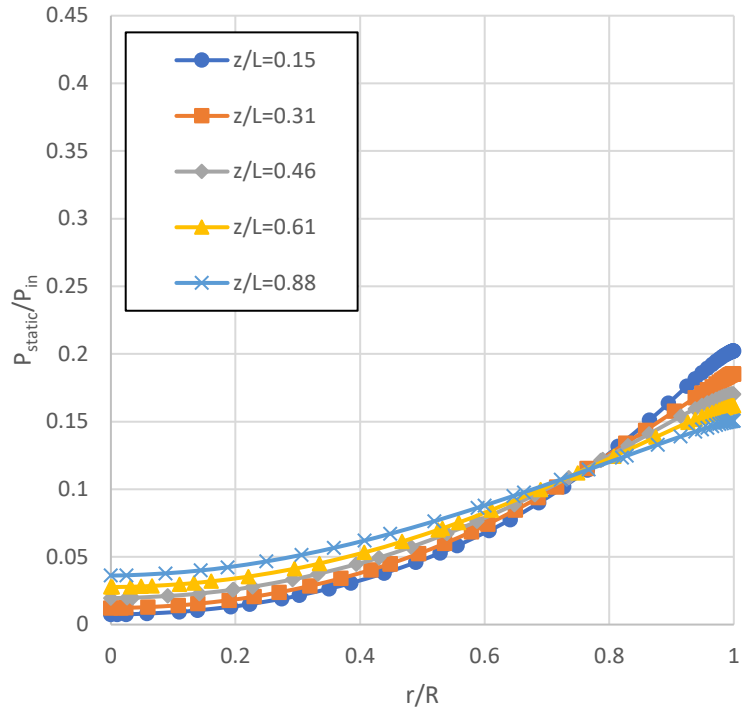
5.2.2. Pressure. Figure 12 (a) shows that the static pressure has a positive gradient in the radial direction and peaks at the wall surface. On the other hand, this gradient decreases as the fluid flows towards the hot end due to the decaying vortex, as shown in Figure 10 (c). For example, at $z/L=0.15$ the difference between the central and the peripheral static pressures is the maximum. This trend indicates that, the angular velocity, hence the static pressure gradient can reach to zero for longer tubes. The radial density profile of the working fluid is shown in Figure 13. It can be observed from the figure that the density increases in the radial direction. This density variation is due to the centrifugal force that pushes the fluid away from the centre. From Figure 12 (b), it can clearly be observed that the total pressure profile and the velocity have the same trend of increasing

in radial direction to peak at the periphery. Then, the pressure decreases to reach the static pressure at the wall surface due to no slip condition. It worth mentioning that, although the velocity magnitude decreases along the tube length, the total pressure increases in this direction. Hence, the static pressure change dominates that of the dynamic pressure as in Eq. 10.

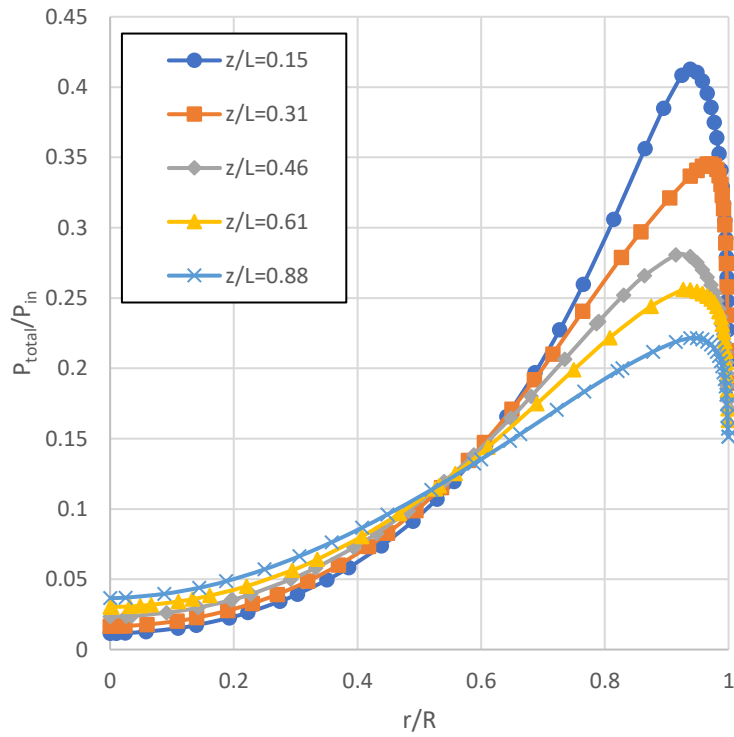
$$P_t = P_s + \frac{1}{2}\rho V^2 \quad (10)$$

5.2.3. Temperature. Figure 14 (a) shows the radial variation of the static temperature at different locations in the VT. The temperature profile has a negative gradient in the radial direction, which indicates heat conduction from the near axis region to the peripheral region. This outcome is due to the contradicting effect of pressure and density on the static temperature as $T=P/(\rho R)$. The increase in the static pressure is not sufficient to accommodate the increase in density, which consequently leads to a decrease in the static temperature. As fluid flows towards the hot outlet, the amount of heat conducted radially decreases due to a lower temperature difference. For instance, at $z/L=0.15$, the radial temperature drop is about 10 K, while at $z/L=0.88$ mm it is about 3 K. On the other hand, static temperature increases in the axial direction, which confirms that the heat is conducted from the hot to the cold outlet side. This heat transfer phenomena cannot be neglected, due to the nature of swirl flow in the VT. Swirl flow significantly increase the contact area and the residence time of fluid layers, hence the heat transfer between them. It worth noting that, the radial temperature drop violates the secondary flow theory. The theory claims that the secondary circulations work as a refrigeration cycle where it absorbs heat from the cold core (center) and reject it to the near wall region.

Figure 14 (b) presents that the total temperature is the minimum at the center and increases in the radial direction. This profile is due to the nature of velocity distribution inside the VT. Despite of the velocity reduction, the total temperature increases in the axial direction. This contradiction is due to conversion of kinetic energy into heat by shear forces. At $z/L=0.88$ mm, near the tip of the valve, the static and the total temperatures are equal because of the stagnation of the fluid at this region. Another remarkable outcome that should be pointed out is that at the near wall region with no slip condition, the static and total temperatures become equal as fluid flow along the tube, which is in agreement with the larger eddy simulation model in[39].



(a)



(b)

Figure 12: Pressure profiles inside the vortex tube at different locations (a) static pressure (b) total pressure.

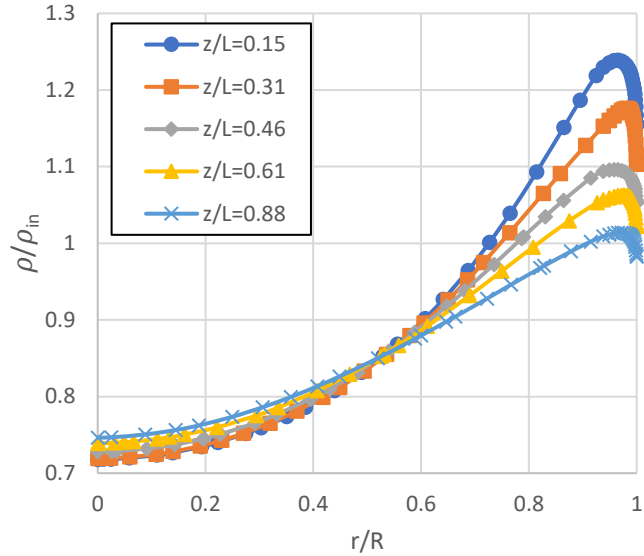
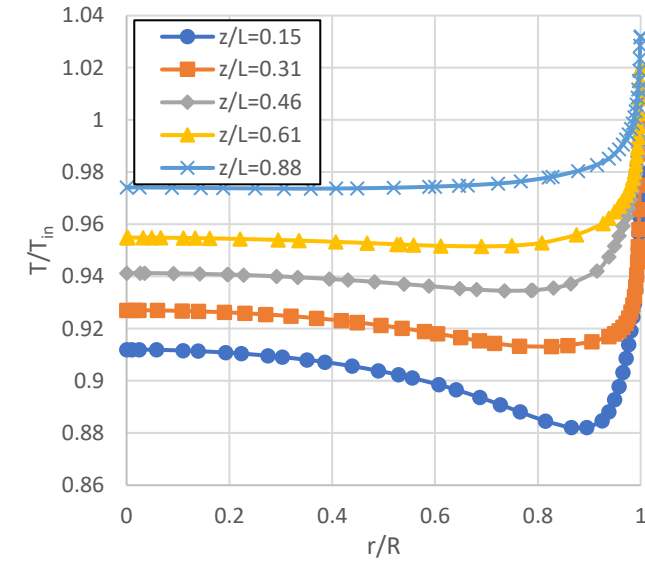


Figure 13: Density profile inside the vortex tube at different locations.

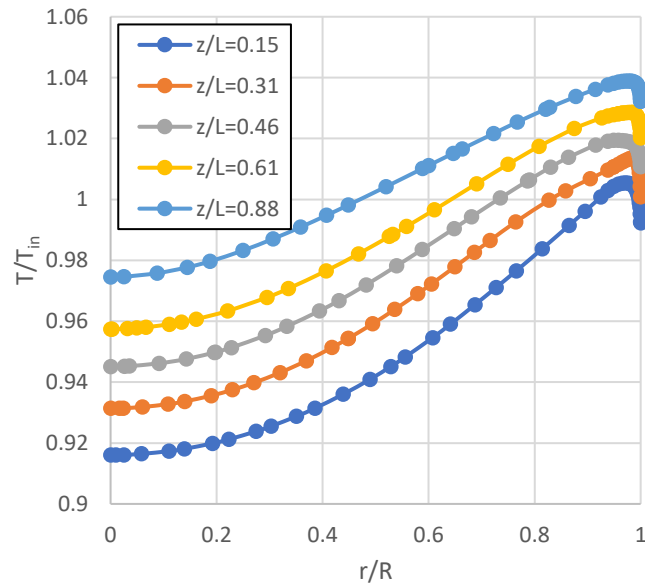
5.3. Effect of Molecular Weight

Figure 15 illustrates the impact of molecular weight of a gas on the outlet temperatures. Overall, it can be seen that the MW can significantly affect the static temperatures, Figure 15 (a), and the cold total temperature, Figure 15 (b), while it approximately has no minute effect on the hot total temperature, Figure 15 (b). Furthermore, increasing the MW leads to a substantial increase in the values of both. the static and total temperatures of the cold outlet. For given VT design conditions, when the molecular weight ratio increases from 0.69 to 1.55, both the static and total cold temperature ratios increase from 0.925 to 0.955, which correspond to 9°C rise in the temperature of the cold fluid. Although the effect of increasing MW has improved the hot static temperature, about 15°C, it shows a minor decrement in the hot total temperature. To properly explain the impact on static and total temperature, one needs to refer to the relation between these temperatures in Equation (11)[49]. The equation above clearly shows that total temperature will significantly be larger than the static temperature at high outlet velocities, which is expected at the hot outlet. It also indicates that the total temperature will approach to the static temperature at low velocities, which is expected at the cold outlet. The expected high velocities at the hot outlet and low velocities at the cold outlet can be seen more clearly in Figure 8. Based on the VT structure, the hot gas leaves near the tube periphery while the cold gas leaves near the center of the tube. As show in Figure 16, the total velocity is high near the tube periphery, and low near the center. The periphery

experience high velocities while the tube center region experiences low velocities due to the tangential nozzle arrangement that cause a strong vortex formation in the VT. It is more difficult to move heavy particles (high MW) compared to light weight particles (low MW). Hence, due to the concept of momentum conservation, as expected high MW particles have lower velocities compared to the low MW particles, as show in Figure 16.



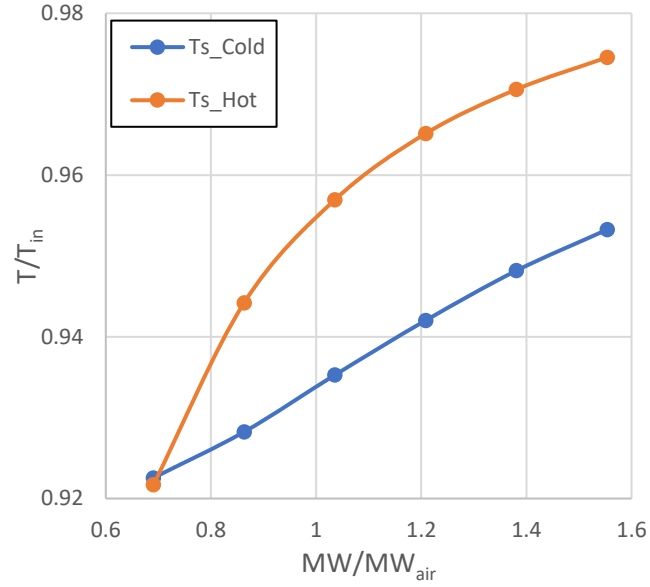
(a)



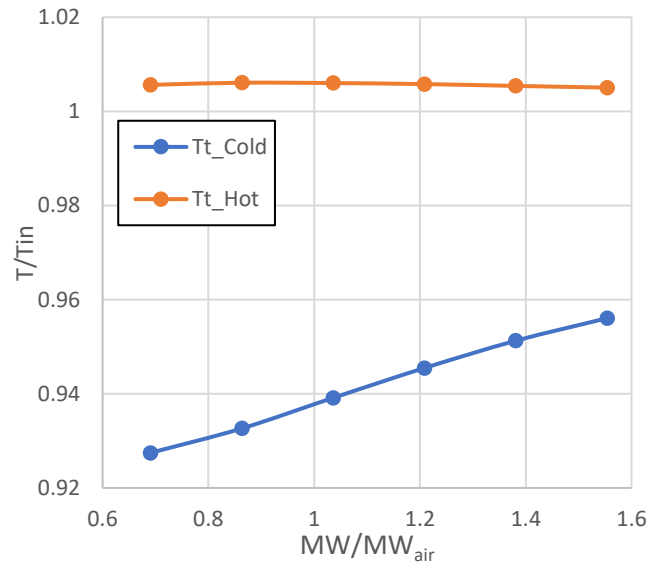
(b)

Figure 14: Temperature profiles inside the vortex tube at different locations (a) static temperature (b) total temperature.

$$T_{Total} = T_{static} + \frac{V^2}{2C_p} \quad (11)$$



(a)



(b)

Figure 15: Effect of molecular weight ratios on dimensionless (a) Static and (b) Total outlet temperatures.

Also, for selected axial location $z/L = 0.63$, it is clear that forced vortex is formed for $0 < r/R < 0.9$, which get crumbles near the tube periphery due to no-slip condition and boundary layer formation.

In more details, the impact of the MW is clearly observed from ideal gas equation in Eq. (4), which shows that MW is directly proportional to static temperature and density while inversely proportional to the static pressure.

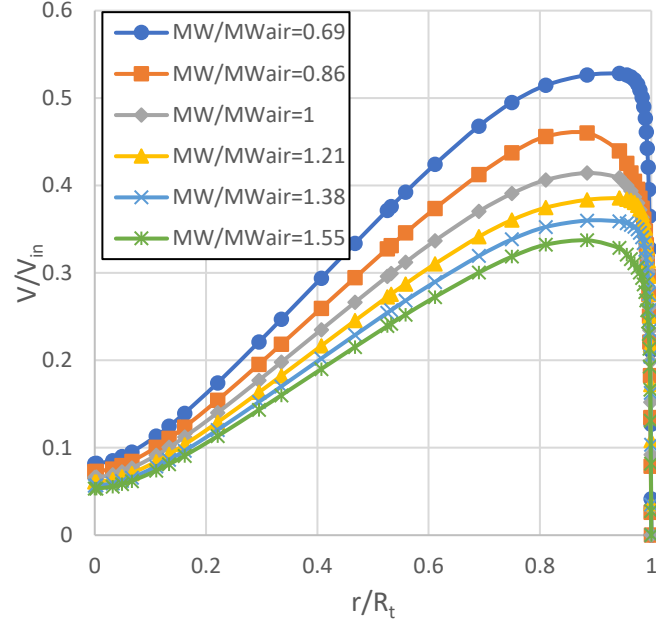


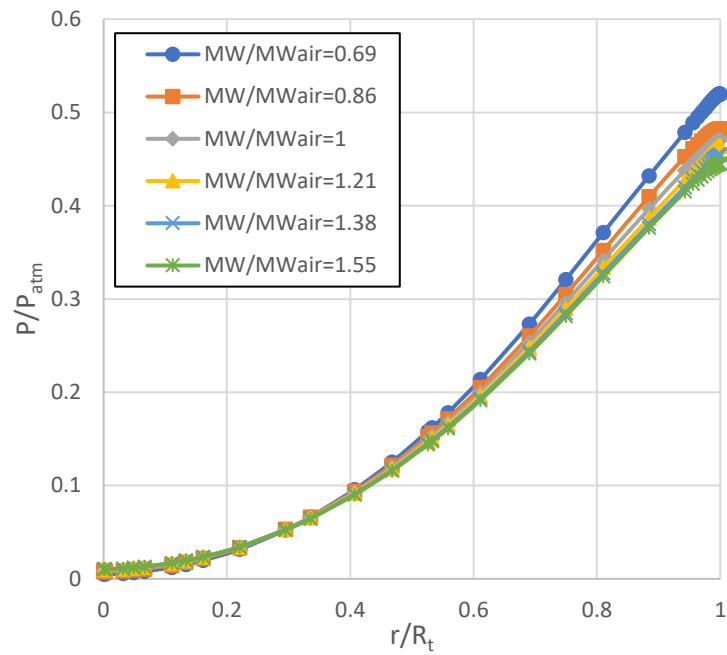
Figure 16: Dimensionless velocity profiles versus dimensionless radial direction plotted at $z/L=0.63$ for various molecular weight ratios.

At a specific axial location of $z/L = 0.63$, the impact of MW on pressure, density and temperature are shown in Figure 17, Figure 18 and Figure 19, respectively. The impact of MW on static and total dimensionless pressure profiles at a fixed axial location of $z/L = 0.63$ is shown in Figure 17. Figure 17 (a) shows the dimensionless static pressure profile in radial direction for different MW ratios. For a fixed MW, Figure 17(a) shows that the dimensionless static pressure increases in radial direction due to the centrifugal force produced by the vortex flow that pushes the gas particles toward the tube. Moreover, it is clear that the dimensionless static pressure decreases at larger MWs, which agrees with the ideal gas law shown in Eq. (4). In Figure 17(b), the dimensionless total pressure increases radially until starts decreasing about the tube periphery. This pressure profile is due to the fact that the total pressure depends on static pressure and fluid velocity as in Eq. (11). While static pressure increases radially, velocity increases then decreases due to the no-slip condition near the periphery. Also, the total pressure decreases as MW increases, which is expected since as MW increases, both the static pressure and the total velocity decrease.

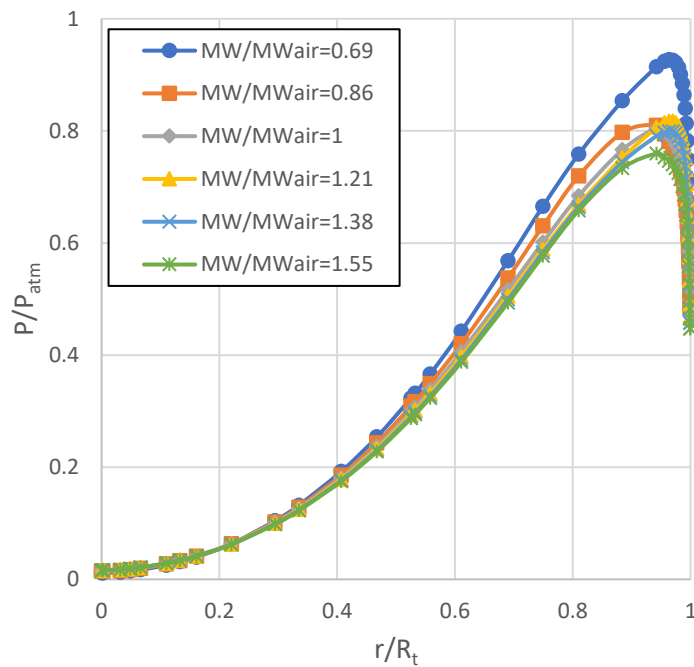
$$P_t = P_s + \frac{1}{2}\rho V^2 \quad (12)$$

Figure 18 shows that density increases in radial direction due to the vortex centrifugal force, which pushes more particles near the tube periphery. An increase in

number of particles leads to an increase in gas density. The figure also shows that density is proportional to MW that is expected as shown in Eq. (4).



(a)



(b)

Figure 17: Dimensionless pressure profiles versus radial direction plotted at $z/L=0.63$ for various molecular weight ratios. (a) Static and (b) Total pressures

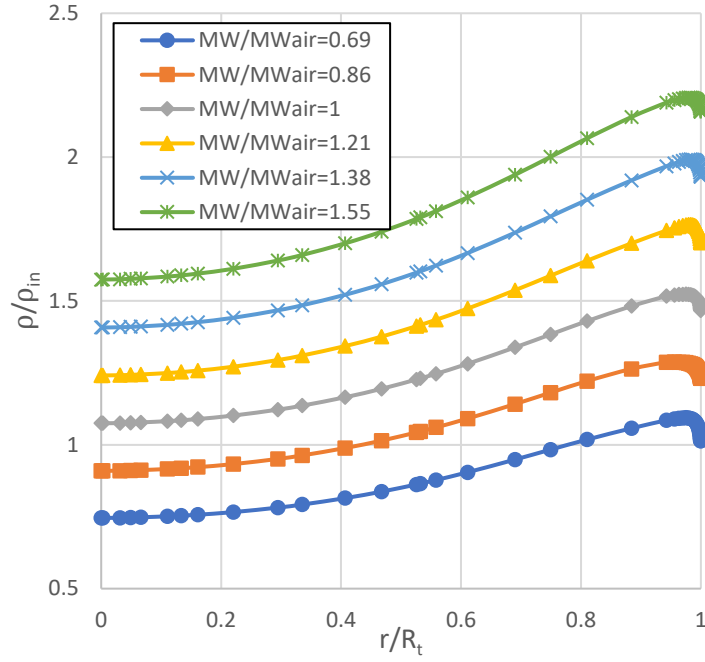
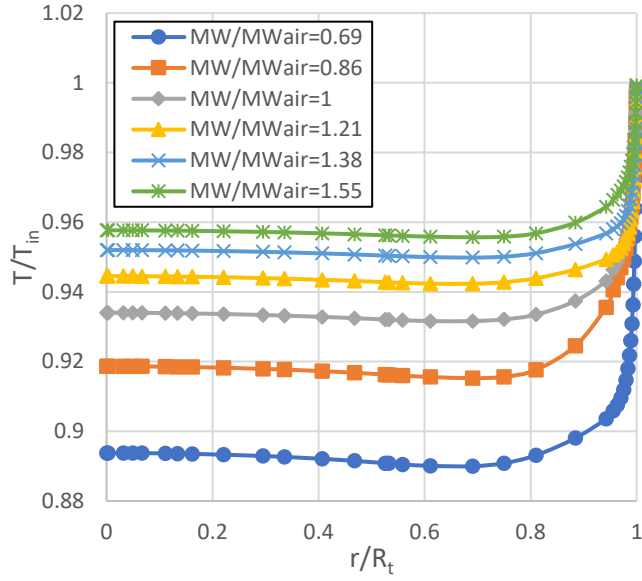
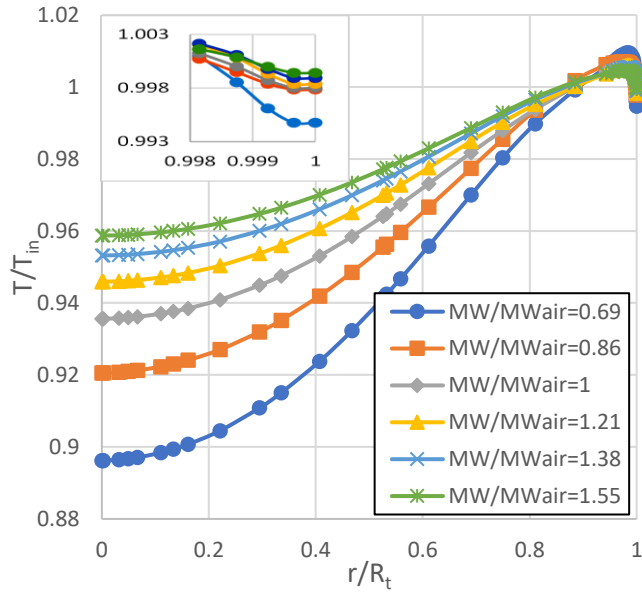


Figure 18: Dimensionless density profiles versus dimensionless radial direction plotted at $z/L=0.63$ for various molecular weight ratios.

Figure 19 shows the dimensionless static temperature profile in radial direction at a specific axial location of $z/L = 0.63$ for different MW ratios. The figure shows that the dimensionless static temperature decreases in radial direction and then increases toward the tube periphery. This profile is dictated by the static pressure and density, which are shaped by the vortex flow centrifugal force. By examining Eq. (4), $\bar{T} = \bar{p}/(\rho R)$ with Figure 17 and Figure 18, it is clear that static pressure (\bar{p}) increases in radial direction while the inverse density ($1/\rho$) decreases, hence a non-monotonic relation for static temperature is expected. These relations yield high static temperature values at the center of the tube and the walls while low in between. The figure also shows that an increase in MW causes a rise in the static temperature for the entire radial axis. It was formulated in the ideal gas equation and confirmed from the figure that the static temperature is directly proportional to MW. On the other hand, in Figure 19 (b), the increase in MW causes a rise in the total temperature within the forced vortex ($0 < r/R < 0.75$). However, outside the forced vortex, predicting the trend is inconsistent. Nonetheless, with proper zooming in Figure 19 (b) close-up, the same trend is observed near the wall as well. The figure also illustrates that the coldest static temperature occurs inside the tube at any MW ratio, which indicates a heat transfer from the center and the wall of the VT to the coldest point region.



(a)



(b)

Figure 19: Dimensionless temperature profiles versus dimensionless radial direction plotted at $z/L=0.63$ for various molecular weight ratios. (a) Static and (b) Total temperatures.

5.4. Effect of Thermal Conductivity

The effect of thermal conductivity (TC) on dimensionless static and total outlet temperatures is shown in Table 3. Although, $k = 1$ is not a realistic TC ratio for gases, it is tested to bring the doubt about the influence of TC to an end. In general, increasing the TC has no effect on the temperature of outlet streams. It can be seen that as the TC increases

from 0.005 to 0.04 the change in temperature is less than 1 Kelvin. A similar trend is observed in Figure 20 that shows the static temperature profile in radial direction. It is clear that the static temperature profile does not significantly change with variation of TC. The temperature profile indicates that small amount of heat transfers from the VT wall and center to the coldest point in the profile. This static temperature profile does not depend on the TC ratios. It depends on the static pressure and density, which are independent from the TC ratios. This conclude that the insignificant heat transfer in radial direction does not justify the energy separation in the vortex tube.

Table 3: Effect of thermal conductivity on outlet temperatures.

k [w/m.k]	k/k_{air} [-]	$T_{s.Cold}$ [K]	$T_{s.Hot}$ [K]	$T_{t.Cold}$ [K]	$T_{t.Hot}$ [K]
0.005	0.207	279.379	286.7418	280.66	301.975
0.01	0.413	278.9891	286.861	280.2953	302.04
0.02	0.826	278.6455	286.9721	279.9728	302.101
0.03	1.24	278.4154	287.0432	279.7557	302.141
0.04	1.653	278.2434	287.0971	279.5931	302.171
1	41.32	276.3433	287.7653	277.7672	302.557

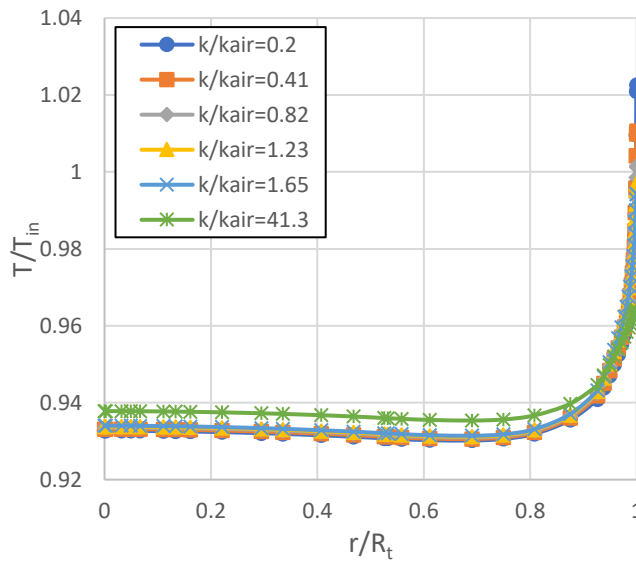


Figure 20: Dimensionless static temperature profiles versus dimensionless radial direction plotted at $z/L=0.63$ for various thermal conductivity ratios.

5.5. Effect of Heat Capacity

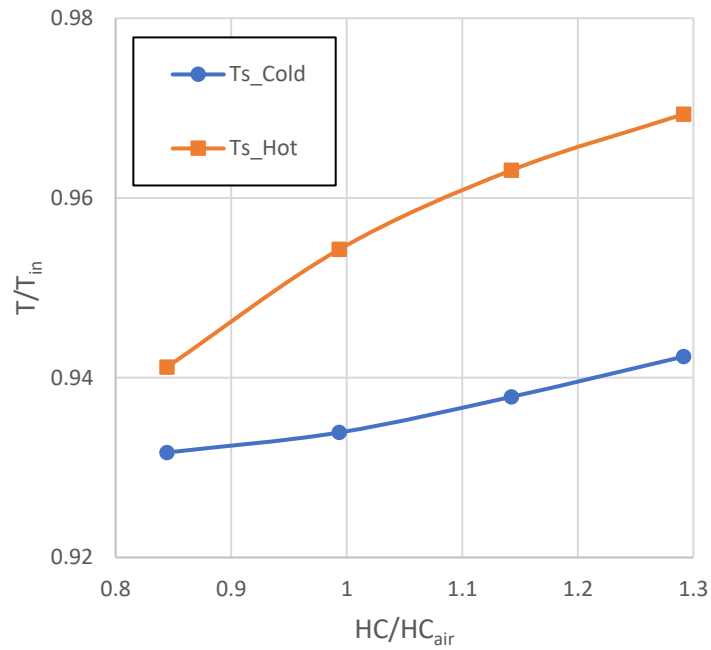
Figure 21 presents the variation of outlet temperature of the VT as a function of heat capacity (HC). Although, the incremental change of the HC causes an increase in the

static and the cold total temperatures, it shows a plateau effect on the hot total temperature. For a moment, noticing the impact of HC on the energy separation could sound confusing, since it is well-known that in steady state operation (like VT operation) the HC does not affect temperature distribution [50]. However, Figure 21 proves that HC has a clear impact on the energy separation in VT tube. This impact is due to the fact that HC represents the amount of energy coming with the fluid through nozzles. When this energy is released inside the VT and forms the vortex flow, it is distributed based on the flow structure and pressure. Therefore, an increase in HC causes an increase in the static temperature as shown in Figure 21 (a). From Figure 21 (b) and Eq. (10), the cold total temperature is directly proportional to the cold static temperature since the cold outlet velocity is small. However, the hot total temperature showed a plateau relation with HC since its value is dominated by the velocity value at the hot outlet. The hot outlet velocity is very high (near sonic) that explains no effect of HC on the hot total temperature. At specific axial location of $z/L = 0.63$, the impact of HC on temperature and pressure are shown in Figure 22 and Figure 23, respectively. The effect of HC on the fluid velocity profile at a specific axial location ($z/L = 0.63$) is shown in Figure 22. It is clear from the figure that HC has a minor effect on velocity. Nevertheless, as HC increases the velocity decreases. This behaviour is due to the fact that the particles with low HC have less ability to store the thermal energy as their internal energy. Hence, this energy is transformed as an increase in the kinetic energy of particles leading to an increase in their velocity.

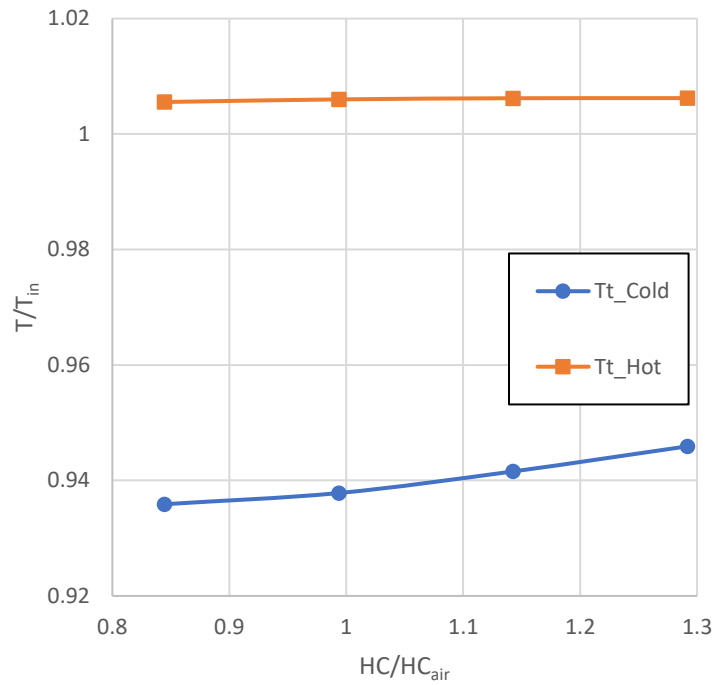
The impact of HC on pressure is shown in Figure 23. As shown in Figure 23 (a), the static pressure decreases as HC increases, which is in agreement with the total velocity results in Figure 22. Because the drop in velocity causes a drop in the centrifugal force that leads to a drop in the static pressure. From Figure 23 (b), the total pressure decreases as HC increases. The total pressure behavior is expected, as per Eq. 11, which indicates that both the static pressure and the total velocity decrease at higher HC.

Figure 24 presents variation of dimensionless temperature profile versus radial axis at a specific axial location of ($z/L = 0.63$) for different HC ratios. From Figure 24 (a), it is clear that the increase in HC rises the static temperatures inside the tube. The rise in the static temperature is due to the increase in the total energy of the gas injected inside the

VT. The increase in HC allows more energy to enter the VT tube, which leads as shown in the close-up of Figure 24 (b), the same trend of forced vortex is observed near the wall too.



(a)



(b)

Figure 21: Effect of heat capacity ratios on dimensionless (a) Static and (b) Total outlet temperatures.

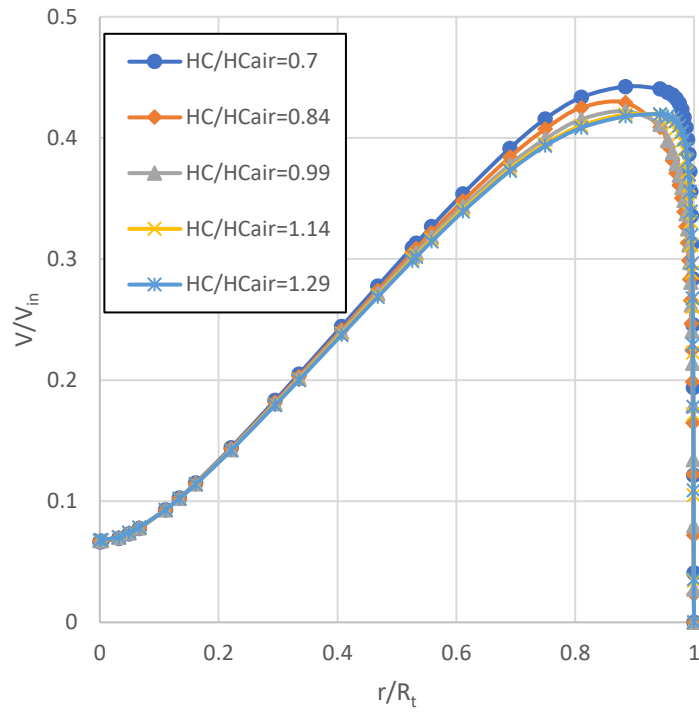
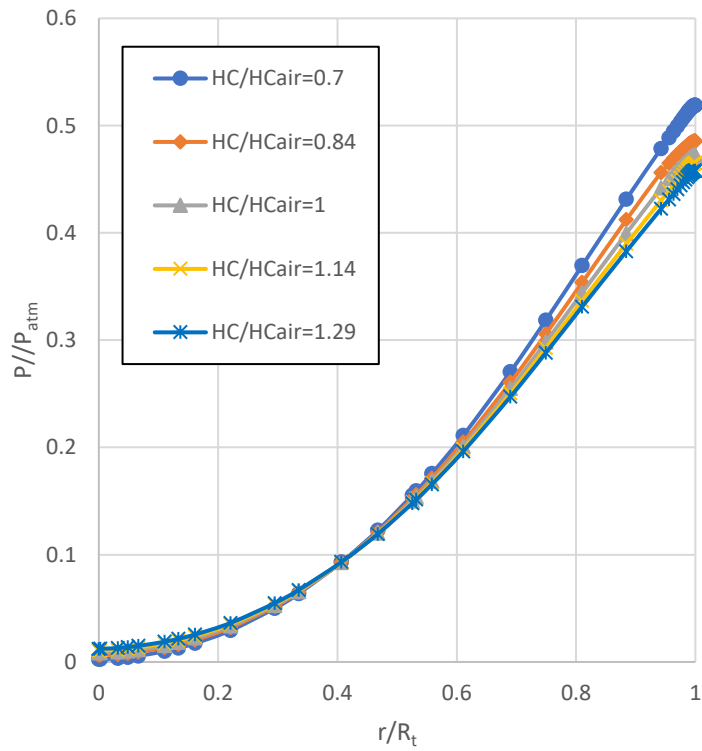
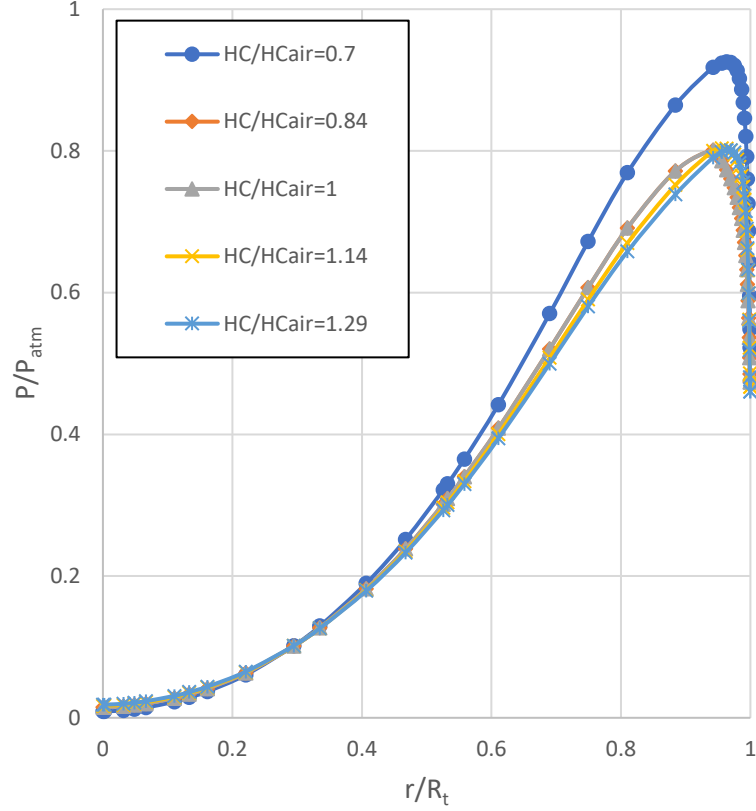


Figure 22: Dimensionless velocity profiles versus dimensionless radial direction plotted at $z/L=0.63$ for various heat capacity ratios.



(a)



(b)

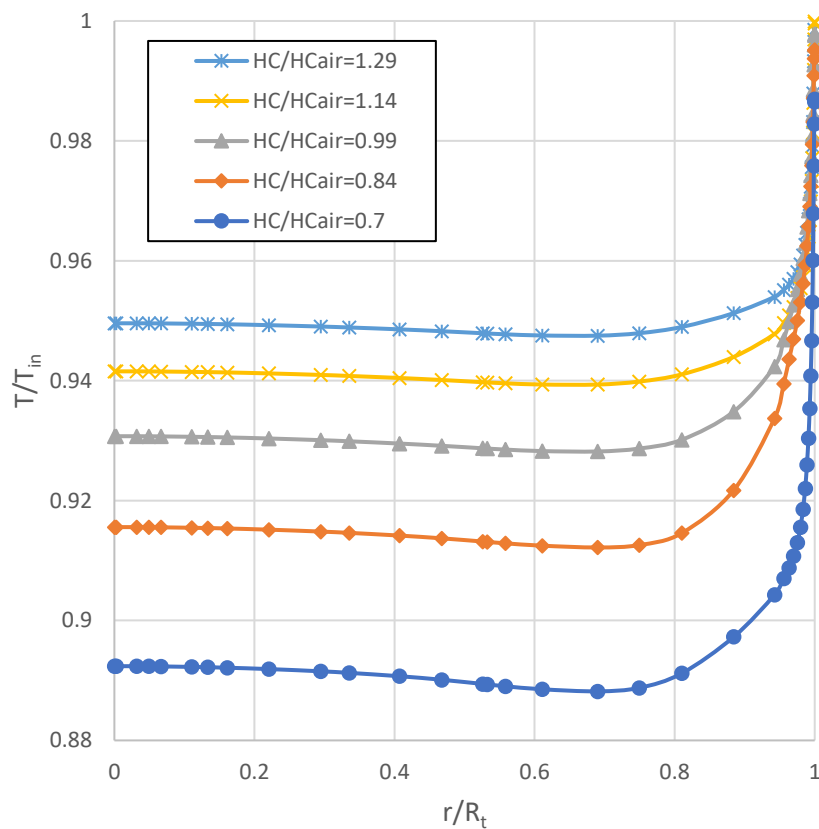
Figure 23: Dimensionless pressure profiles versus dimensionless radial direction plotted at $z/L=0.63$ for various heat capacity ratios. (a) Static and (b) Total pressures.

5.6. Effect of Dynamic Viscosity

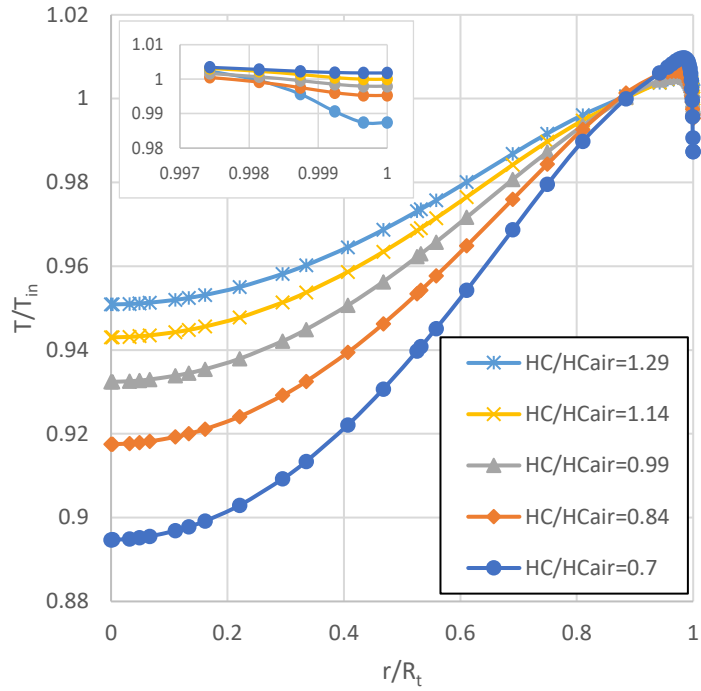
Figure 25 exhibits the impact of the dynamic viscosity on the VT outlet temperatures. The figure shows that increasing dynamic viscosity (DV) increases temperature difference between cold and hot outlets (i.e., improves energy separation). As the DV increases, the hot outlet temperatures (static and total) increase, while the cold side decrease. More specifically, when the DV ratio increases from 0.3 to 4.3, the hot end witnesses sharp increase in the static temperature, $\Delta T \cong 12\text{ }^\circ\text{C}$, and mild increase in the total temperature, $\Delta T \cong 4\text{ }^\circ\text{C}$. Also, both the static and the total cold temperatures substantially decrease with the increase in DV, until it reaches $\mu/\mu_{air} = 3.5$. Beyond DV ratio of 3.5, the change in outlet temperatures is minute and could be neglected. The temperatures of the cold stream drop about $23\text{ }^\circ\text{C}$ between $\mu/\mu_{air} = 0.3$ and $\mu/\mu_{air} = 3.5$. This could be another justification on why helium, which has the highest viscosity as shown in Table 2, gives the best temperature separation performance.

To properly understand the impact of DV on energy separation, the velocity, pressure, density, and temperature profiles that are examined in Figure 26, Figure 27, Figure 28 and Figure 29, respectively. Figure 26 shows that the dimensionless total velocity increases radially until a maximum value, then decreases until no-slip condition at the tube wall. The figure also shows that as dynamic viscosity ratio increases, the viscous forces diffuse toward the tube center. Hence, as DV ratio increases, the maximum velocity decreases while velocity at the centre region increases.

Figure 27 shows that as DV increases, the dimensionless pressure increases near the center while decreases near the periphery. This effect occurs due to the momentum transfer from periphery to the tube center region. The drop in the static pressure near the periphery causes the density a dramatic drop near periphery and an increase near the center region, as shown in Figure 28. This behaviour of density can be explained with the high pressure at the center and low pressure at the wall.

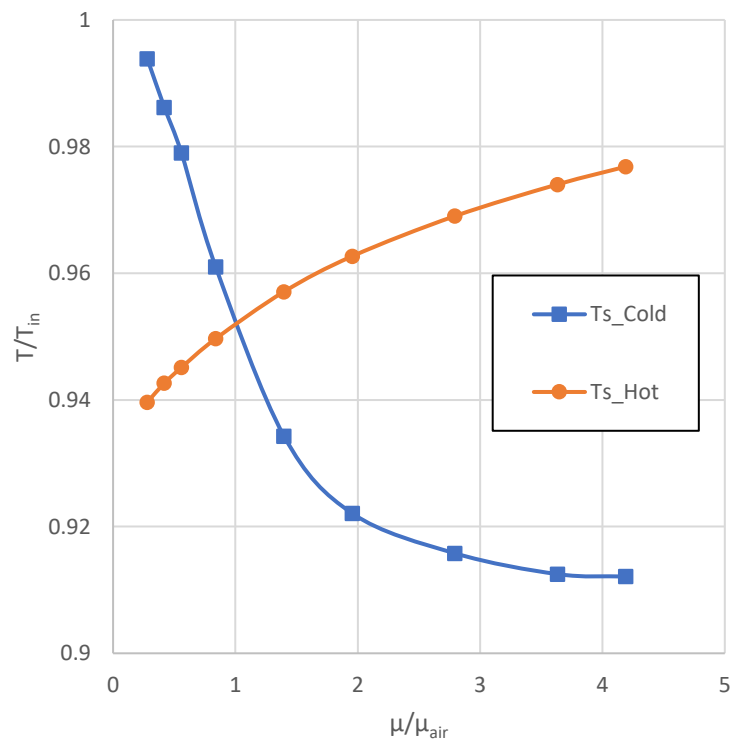


(a)

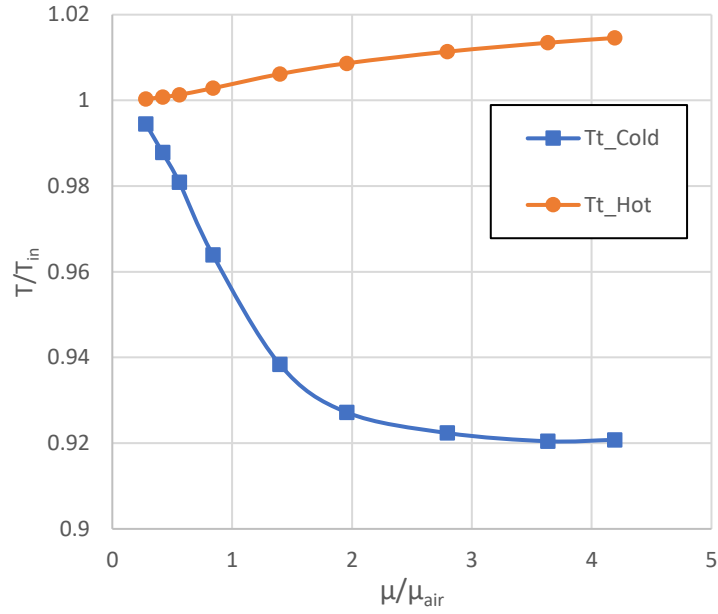


(b)

Figure 24: Dimensionless temperature profiles versus dimensionless radial direction plotted at $z/L=0.63$ for various heat capacity ratios. (a) Static and (b) Total temperatures.



(a)



(b)

Figure 25: Effect of dynamic viscosity ratios on dimensionless (a) Static (b) Total outlet temperatures.

Figure 29(a) shows the dimensionless static temperature profile in radial direction for different DV ratios. The dimensionless static temperature decreases slightly in radial direction until a minimum value of around $r/R = 0.75$, after which it starts increasing toward the tube periphery. The shape of this profile is dictated by the static pressure and density, which are shaped by the vortex flow centrifugal force.

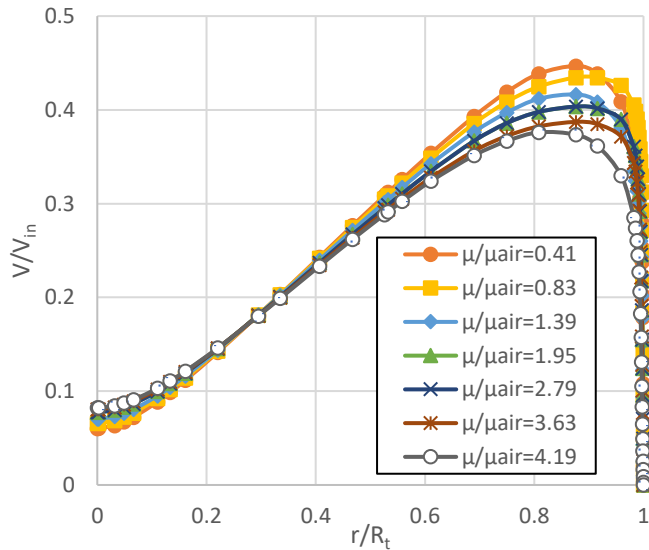
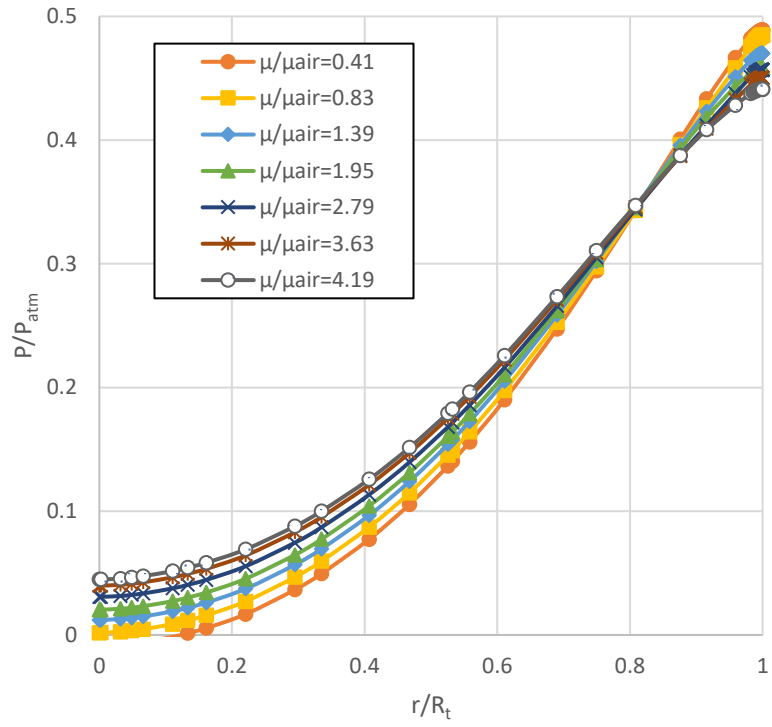
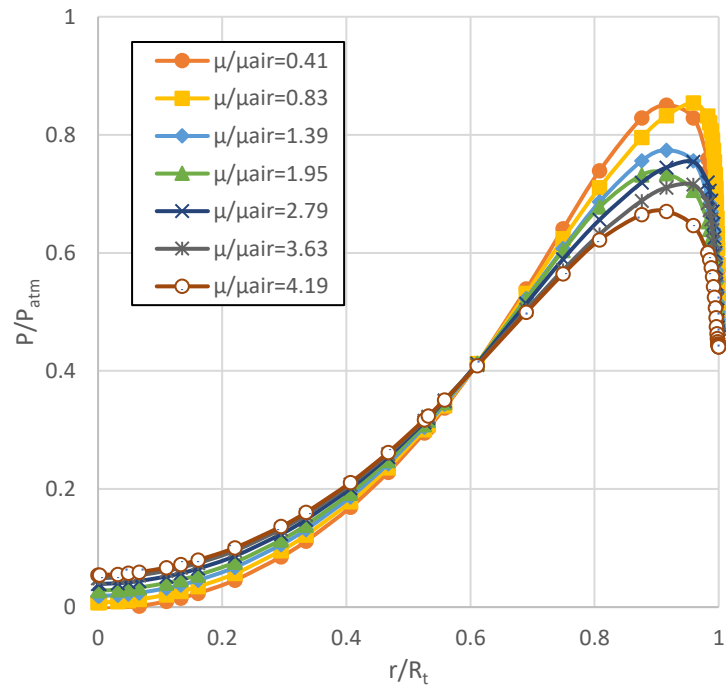


Figure 26: Dimensionless velocity profiles versus dimensionless radial direction plotted at $z/L=0.63$ for various viscosity ratios.



(a)



(b)

Figure 27: Dimensionless pressure profiles versus dimensionless radial direction plotted at $z/L=0.63$ for various dynamic viscosity ratios. (a) Static and (b) Total pressures.

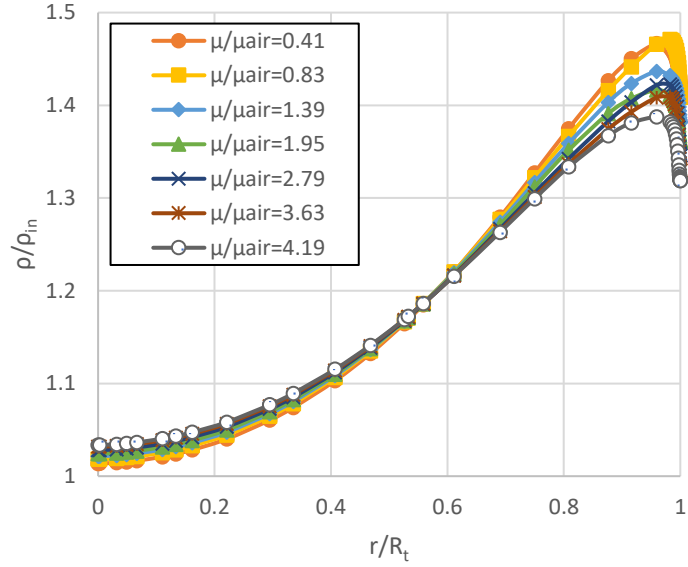
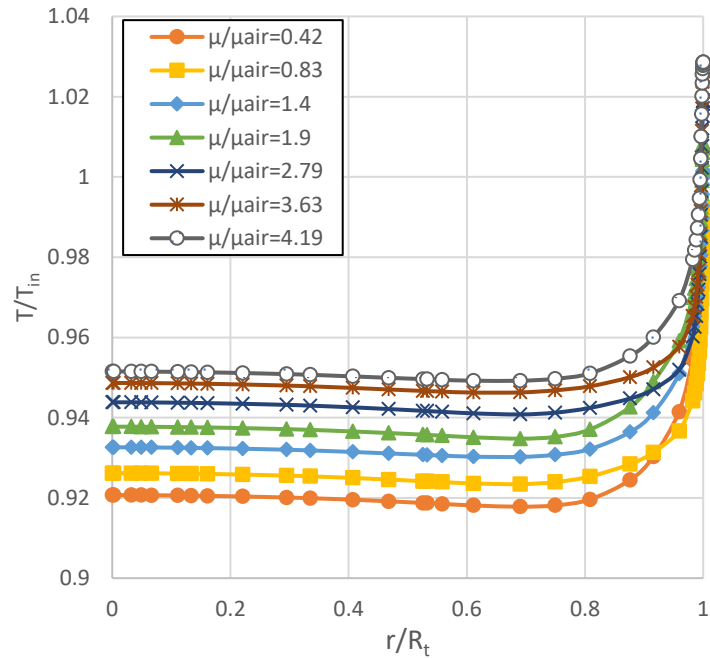
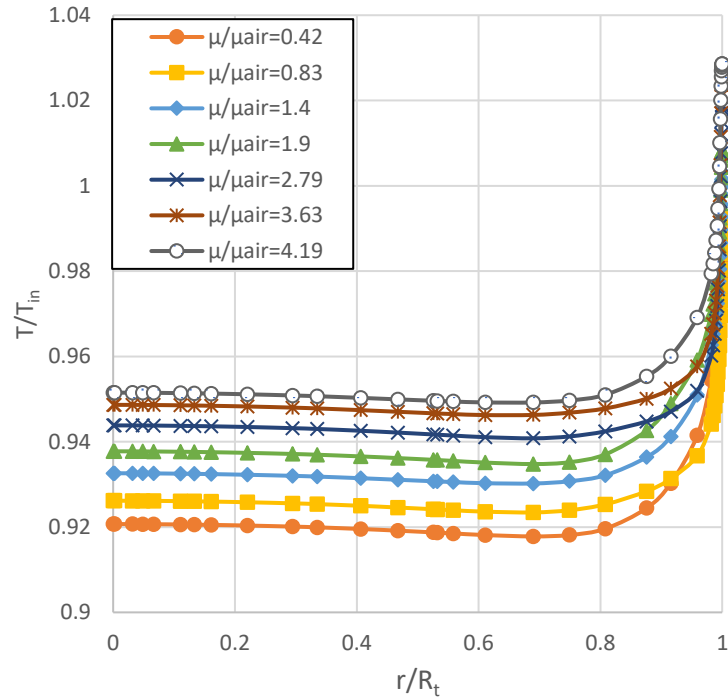


Figure 28: Dimensionless density profiles versus dimensionless radial direction plotted at $z/L=0.63$ for various dynamic viscosity ratios.

Figure 29 reveals that with viscosity and reaches a slightly higher value than the near axis temperature. From the total temperature profile in Figure 29(b), escalating the value of dynamic viscosity rises the total temperature along the radius of the tube. Moreover, as long as the dynamic viscosity ratio is less than 1.95, the temperature profile follows the same trend as the velocity profile, which decreases near the wall.



(a)



(b)

Figure 29: Dimensionless temperature profiles versus dimensionless radial direction plotted at $z/L=0.63$ for various dynamic viscosity ratios. (a) Static and (b) Total temperatures.

5.7. Effect of Tube Diameter

Figure 30 shows the impact of changing the tube's diameter on the heating performance of the vortex tube. This graph is plotted by monitoring the hot outlet pressure that gives the maximum heating rate at each diameter ratio. It can be noticed that as the diameter ratio increases, the heating capacity ratio increases until it reaches an optimum value 0.095 at diameter ratio 0.82; then, it deteriorates to become 0.055 at $d/D=2.0$. The reason of having this optimum value is the radial expansion of the tube's volume that leads to the non-monotonic variation of the static hot temperature, which consequently affect the total temperature, Figure 31. As for the temperature rise, when the diameter ratio increases from 0.69 to 0.82 the drop of density values overshadows that of pressure values, Figure 32 and Figure 33. However, with regard to the temperature drop, after $d/D=0.82$ the pressure drop overshadow the density drop; consequently, static temperature decreases. It is worth mentioning that the radial expansion of the tube's body relieves the congestion of the fluid particles at the periphery of the tube; thus, decreases the viscous heating effect in the near wall region which in turn contribute to decreasing the static temperature at the hot end. Finally, one could claim that the hot mass flow rate could also be a reason of this trend,

however, as shown in Figure 34, the change of the hot mass flow rate opposes that of the heating capacity which means it acts against the improvement of the heating capabilities of the vortex tube.

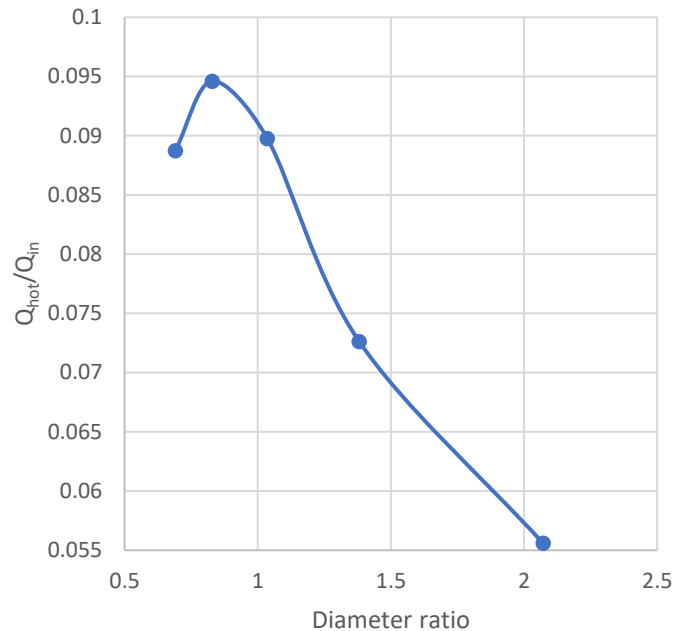


Figure 30: Variation of heating capacity with tube diameter.

Figure 35 depicts how the cooling rate of the vortex tube is altered by the incremental change of tube diameter. This graph is plotted by monitoring the hot outlet pressure that give the maximum heating rate at each diameter ratio. When the diameter ratio increases from 0.69 to 0.82, the cooling capacity ratio increases from 0.088 to 0.094; after that, it starts falling until it reaches 0.05 at $d/D=2.0$. The reason of this trend is mainly the cold mass variation and tediously the static temperature variation within the cold nozzle, Figure 34 and Figure 36. Going into details, although the static temperature increases when diameter ratio increases from 0.68 to 0.82, which could cause deterioration of the cooling capacity, the jump of the mass flow rate within this range of diameter ratio dominates this temperature rise and improves the cooling capacity of the vortex tube. On the other hand, the continuous rise of the static temperature combined with drop of the cold mass flow rate after $d/D=0.82$ crumble the cooling efficiency of the vortex tube. Two phenomena lay behind this behavior of the mass flow rate and the cold static temperature. The first one is the increase of the tube capacity which allow it to hold more fluid and as a result decreases

the cold flow rate. On the other hand, the continuous rise of the static temperature combined with drop of the cold mass flow rate after $d/D=0.82$ crumble the cooling efficiency of the vortex tube. Two phenomena lay behind this behavior of the mass flow rate and the cold static temperature. The first one is the increase of the tube capacity which allow it to hold more fluid and as a result decreases the cold flow rate. The second phenomenon is the fluid compression from the main tube to the cold tube, Figure 37. According to the isentropic compression equation (13), increasing the volume of the main tube will inevitably leads to an increase in the cold static temperature in the cold outlet nozzle.

$$\frac{T_2}{T_1} = \left(\frac{V_1}{V_2}\right)^{\frac{\kappa-1}{\kappa}} \quad (13)$$

5.8. Effect of Tube Length

Figure 38 shows the variation of the vortex tube heating performance as a function of the tube length. This graph is plotted by monitoring the hot outlet pressure that gives the maximum heating rate at each length ratio. It can be seen that as the length ratio increases,

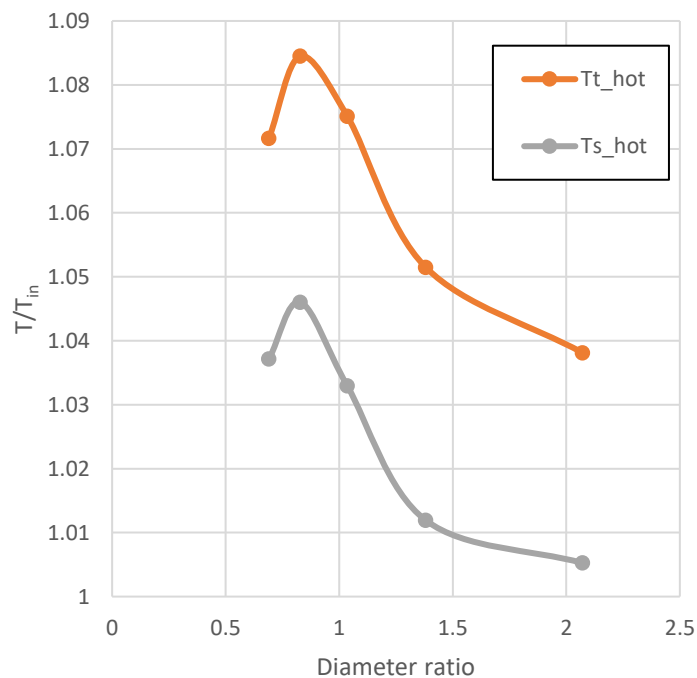


Figure 31: Effect of diameter ratio on hot outlet temperature.

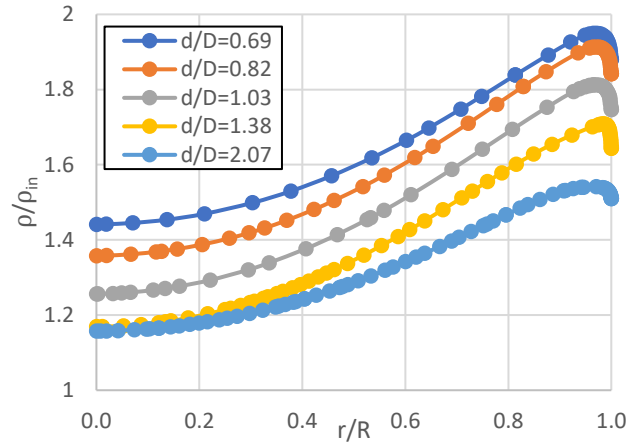


Figure 32: Effect of diameter ratio on the density values inside the flow domain.

the heating ratio of the vortex tube increases until it reaches an optimum value 0.091 at $l/L=1.2$; then, it plateaus at 0.09. This variation is attributed to the change of the hot static temperature, subsequently hot total temperature, and the hot mass flow rate, Figure 39 and Figure 40. Going into details, the extension of the tube length from 80mm to 100mm increases the residence time of the fluid and the contact area between fluid layers which amplify the impact of viscous heating inside the vortex tube. This phenomenon increases the static temperature inside the flow domain, Figure 41. This rise of temperature values overshadows the drop in the mass flow rate values which is an inevitable results of length

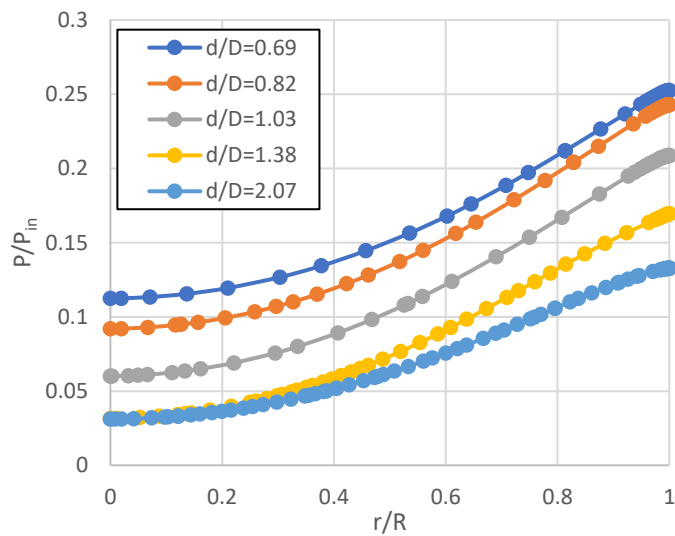


Figure 33: Effect of diameter ratio on cold temperature.

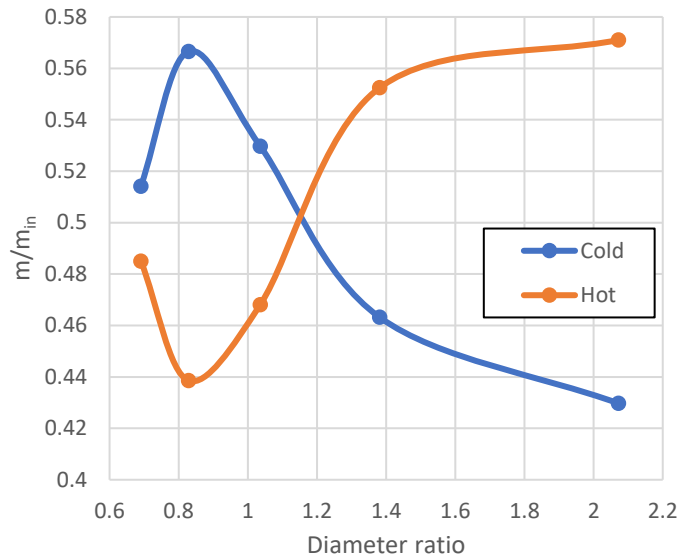


Figure 34: Effect of diameter ratio on the mass flow rate.

extension that increases the flow resistance and the increases the flow resistance and the volumetric capacity of the main tube. On the other hand, when $l/L=1.4$ or more, the progressive increase of the static temperature combined with the progressive decrease of the mass flow rate causes the heating capacity to plateau after these length ratios. It is worth mentioning that the slight drop of the static temperature at $l/L=1.4$ is due to the fact that the maximum heating capacity was achieved at a pressure smaller than that of $l/L=1.2$.

The line graph shown in Figure 42 illustrates how the cooling rate of the vortex tube changes when the length ratio increases. This graph is plotted by monitoring the hot outlet pressure that give the maximum heating rate at each length ratio. Overall, the variation of the cooling capacity seems to be non monotonic as it shows the best performance 0.0922 at $l/L=1.2$ and then it plateaus at 0.09. Increasing the length of the tube makes the cold total temperature follow the same trend as the cold mass flow rate, Figure 40 and Figure 43. Looking at the details, the increase in the mass flow rate conceals that of cold total temperature which improve the cooling capability of the vortex tube. However, after $l/L=1.4$ the tedious increase in the values of these two parameters, about 0.05 in mass and 0.005 in temperature, level out the cooling rate at approximately 0.09. Two phenomena lay behind this behavior of the mass flow rate and the cold total temperature. The first one is the increase of the pneumatic resistance of the main tube which decreases the amount of

fluid flow through the hot end; accordingly, increases it at the cold end. This happens when length ratio increases from 0.8 to 1.2. The second phenomenon is the fluid compression from the main tube to the cold tube, Figure 44. According to the isentropic compression equation (13), increasing the volume of the main tube will inevitably leads to an increase in the cold static temperature.

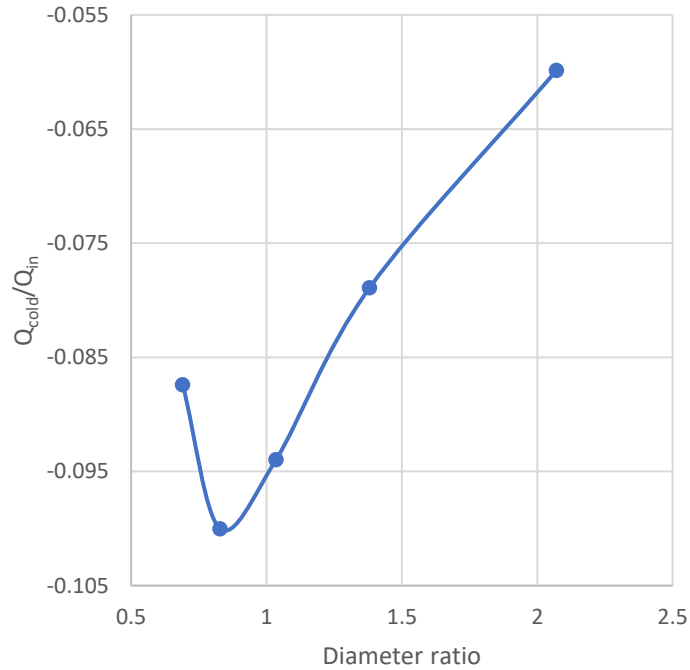


Figure 35: Variation of cooling capacity with tube diameter.

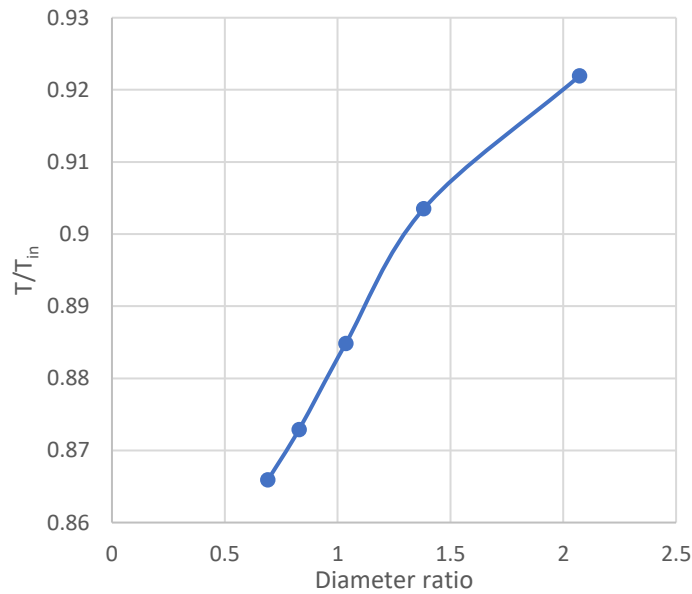


Figure 36: Effect of diameter ratio on cold temperature.

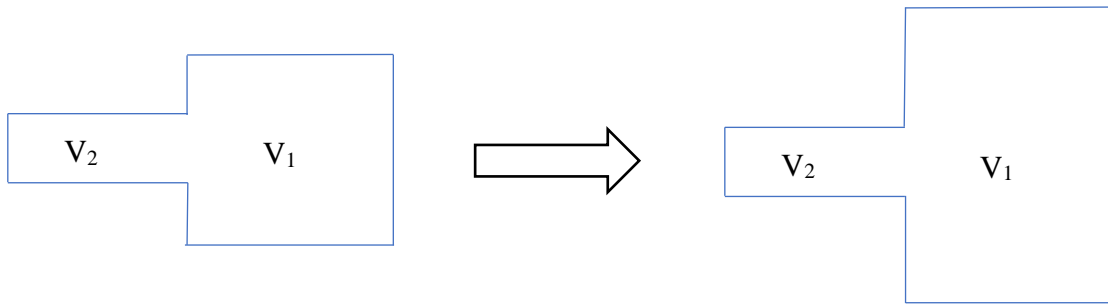


Figure 37: Effect of tube length on cooling capacity.

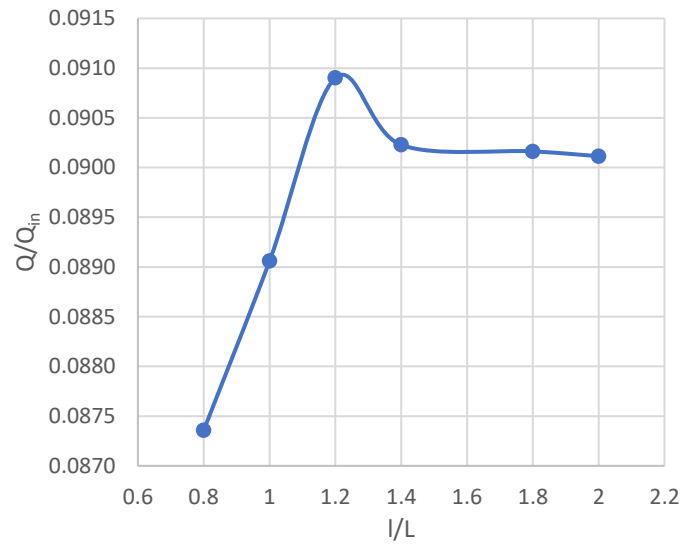


Figure 38: Effect of length ratio on heating capacity.

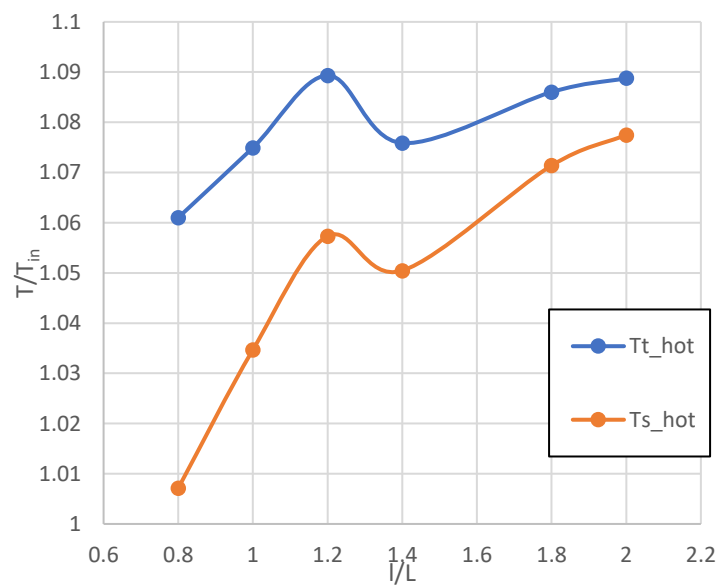


Figure 39: Effect of length ratio on hot outlet temperature.

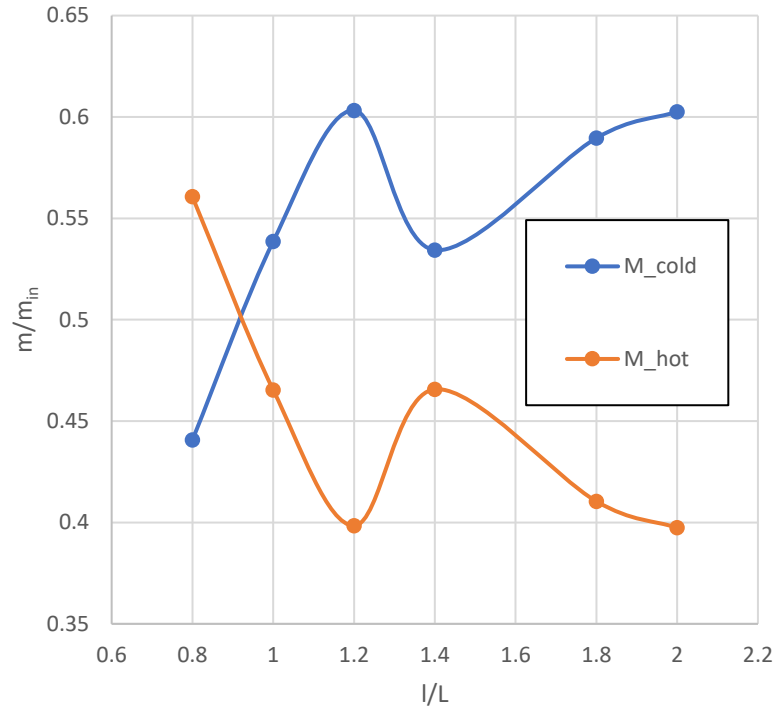


Figure 40: Effect of length ratio on mass flow rate.

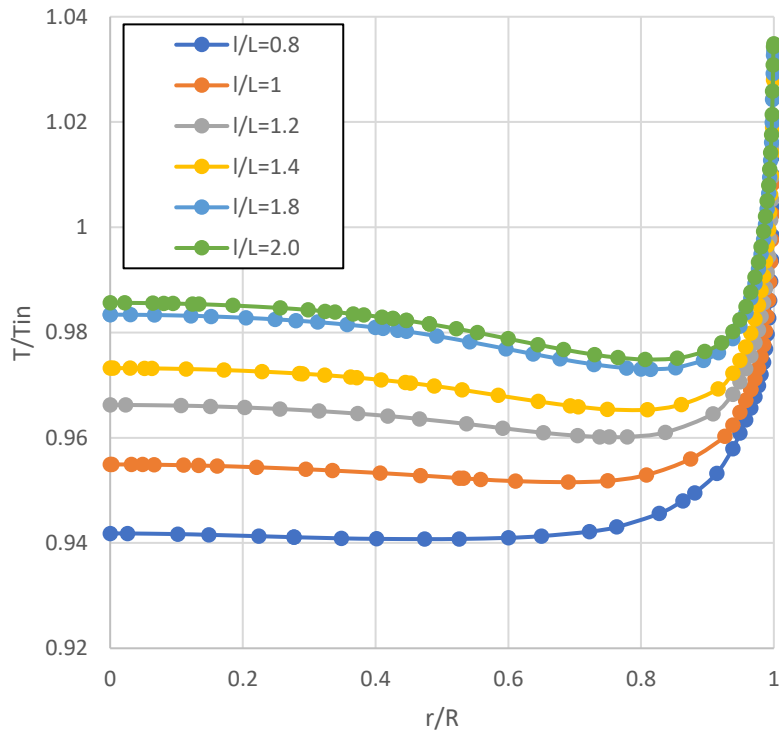


Figure 41: Effect of length ratio on static temperature.

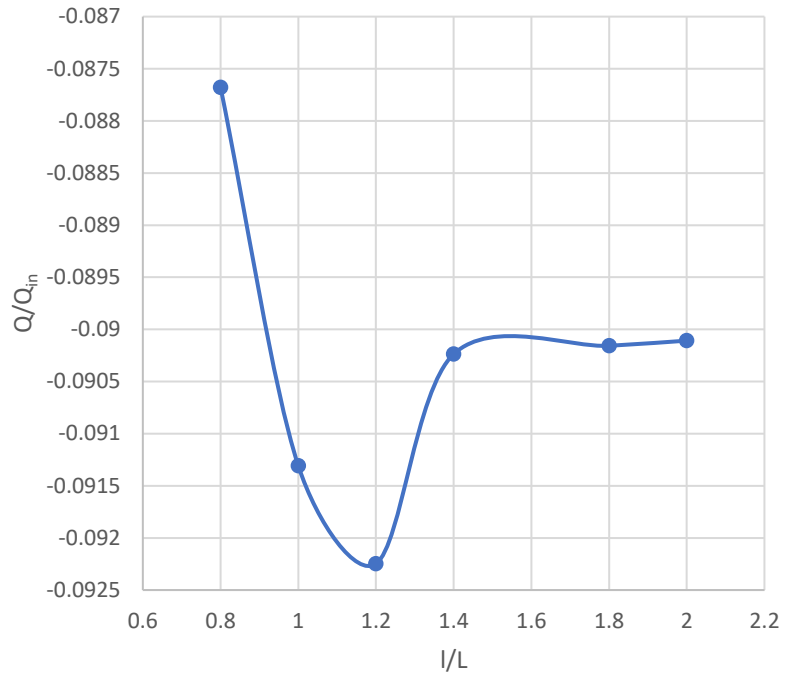


Figure 42: Effect of tube length on cooling capacity.

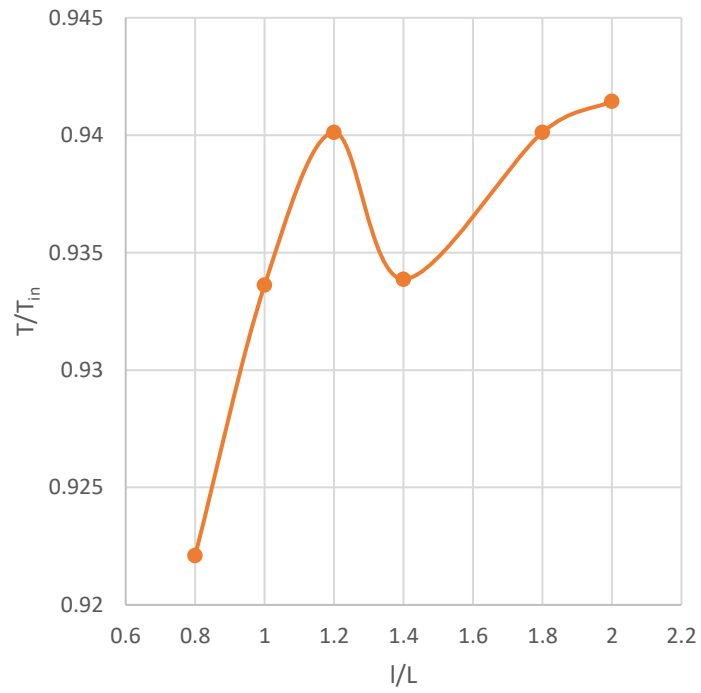


Figure 43: Effect of tube length on cold total temperature.

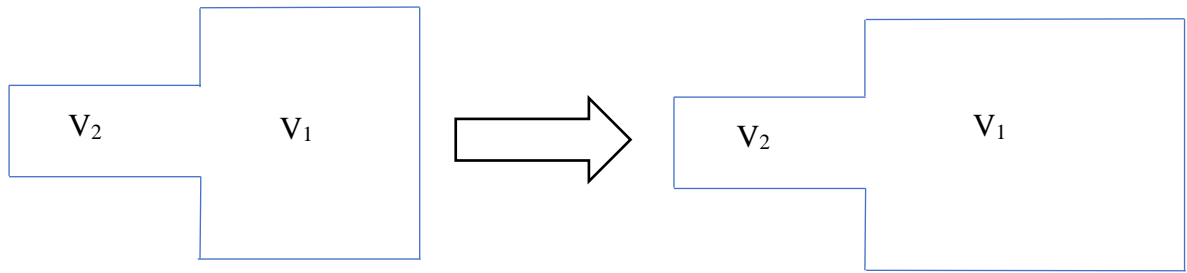


Figure 44: Demonstration of isentropic compression phenomenon.

Chapter 6. Conclusion and Future Work

A series of Computational Fluid Dynamic simulations are conducted to investigate the temperature separation phenomenon in a vortex tube using five different gases, namely helium, carbon dioxide, air, oxygen and nitrogen; besides, the effect of gas properties such as molecular weight, heat capacity, thermal conductivity and dynamic viscosity on the outlet temperatures. Furthermore, the flow field inside a real RHVT is examined also where Velocity, pressure, and temperature radial profiles are plotted at various tube locations. The results indicate the following:

- The SST $k - \omega$ turbulence model with a proper wall condition ($y^+ < 5$) shows an acceptable capability to predict the experimental data.
- Viscous dissipation needs to be considered when modeling vortex tube and its impact appears mainly at the vortex generation region.
- At the near wall region, the large velocity gradient of the tangential component enhances the transfer of the centrifugal force between fluid layers due to the shear stress and viscosity of the fluid.
- Helium yields the maximum separation while carbon dioxide the lowest.
- Increasing the molecular weight or the heat capacity of the working fluid decreases velocity, static pressure, and total pressures in the peripheral region of the tube only. Similarly, increasing the dynamic viscosity decreases the velocity and pressures in the peripheral region, while increases them in the near axis region.
- Varying the thermal conductivity shows no impact on the temperature inside the tube or at the outlets. Hence, the heat transfer in radial direction cannot be used to justify the energy separation in the vortex tube.
- The dynamic viscosity of the fluid plays a crucial role in energy separation in the vortex tube as long as $\mu/\mu_{air} < 3.5$, since it allows greater static temperature along the radial direction.
- The relationship between cold mass fraction and outlet temperatures is non-monotonic. Therefore, an optimum value of the maximum hot and the minimum cold temperatures should be carefully evaluated.

- The flow structure inside RHVT consists of a forced vortex that occupies a big portion of the fluid domain (from $r/R=0$ to 0.9) and a free vortex that exists at the periphery of the tube (from $r/R=0.9$ to 1).
- In spite of the fact that pressure in the peripheral region is higher than that in the near axis region, the radial velocity component is very small due to the centrifugal force that pushes the fluid particles away from the center.
- The relation between the static pressure and temperature is not directly proportional. Therefore, in the high-pressure region a low static temperature occurs, while in the low-pressure region a high static temperature. This indirect relation emphasizes the fact that the static pressure difference between center and the periphery of the tube cannot be considered as a cooling mechanism.
- Fluid expansion is the only cooling mechanism that is observed in the VT as the minimum temperature occurs only at the vortex generator region. Consequently, it is more convenient to regard a VT as a heater with heat separation capability.

As a future work, there are several ideas need to be investigated about about vortex tube such as:

- 1- Performance of the tube when it is used to separate a mixture of gases.
- 2- Its capability in natural gas liquification.
- 3- Effect of valve shape at the hot outlet.
- 4- Effect of the nozzle shape, arrangement, and number.

References

- [1] G. Ranque, "Experiments on expansion in a vortex with simultaneous exhaust of hot air and cold air," *J. Phys. Radium*, vol. 4, no. 7, pp. 112-114, 1933.
- [2] R. Hilsch, "The use of the expansion of gases in a centrifugal field as cooling process," *Review of Scientific Instruments*, vol. 18, no. 2, pp. 108-113, 1947.
- [3] B. Alsayyed, M. O. Hamdan, and S. Aldajah, "Vortex Tube Impact on Cooling Milling Machining," in *ASME International Mechanical Engineering Congress and Exposition*, 2012, vol. 45196: American Society of Mechanical Engineers, pp. 773-776 .
- [4] P. D. Kuila and S. Melkote, "Effect of minimum quantity lubrication and vortex tube cooling on laser-assisted micromilling of a difficult-to-cut steel," *Proceedings of the Institution of Mechanical Engineers, Part B: Journal of Engineering Manufacture*, vol. 234, no. 11, pp. 1422-1432, 2020.
- [5] X. Zhai, "Research on the application of vortex tube type of cooling jacket in coal mine," in *AIP Conference Proceedings*, 2017, vol. 1864, no. 1: AIP Publishing LLC, p. 020220 .
- [6] M. Izadi, A. M. Makvand, E. Assareh, and F. Parvaz, "Optimizing the design and performance of solid–liquid separators," *International Journal of Thermofluids*, vol. 5, p. 100033, 2020.
- [7] J. Chen, W. Yu, H. Zhu, and Z. Cheng, "Investigation of the convex mirror cooling of a transversely excited atmospheric (TEA) CO₂ coaxial output unstable resonator laser," *Journal of Optics A: Pure and Applied Optics*, vol. 11, no. 1, p. 015502, 2008.
- [8] M. O. Hamdan, A. Alawar, E. Elnajjar, and W. Siddique, "Feasibility of Vortex Tube Air-Conditioning System," in *ASME/JSME Thermal Engineering Joint Conference*, 2011, vol. 38921, p. T20004 .
- [9] A. N. Shmroukh, M. Attalla, and A. A. E.-N. Abd El, "Experimental investigation of a novel sea water desalination system using ranque-hilsch vortex tube," *Applied Thermal Engineering*, vol. 149, pp. 658-664, 2019.
- [10] Y. Xue, J. R. Binns, M. Arjomandi, and H. Yan, "Experimental investigation of the flow characteristics within a vortex tube with different configurations," *International Journal of Heat and Fluid Flow*, vol. 75, pp. 195-208, 2019.
- [11] B. M. Dobratz, "Vortex tubes, a bibliography," California. Univ., Livermore. Lawrence Radiation Lab., 1964 .
- [12] M. Kurosaka, "Acoustic streaming in swirling flow and the Ranque—Hilsch (vortex-tube) effect," *Journal of Fluid Mechanics*, vol. 124, pp. 139-172, 1982.
- [13] A. Gutsol, "The ranque effect," *Physics-Uspeski*, vol. 40, no. 6, p. 639, 1997.
- [14] B. Ahlborn, J. Camire, and J. Keller, "Low-pressure vortex tubes," *Journal of Physics D: Applied Physics*, vol. 29, no. 6, p. 1469, 1996.
- [15] C. D. Fulton, "Ranque's tube," *J. ASRE Refrigerating Engng*, 1950.
- [16] R. Deissler and M. Perlmutter, "Analysis of the flow and energy separation in a turbulent vortex," *International Journal of Heat and Mass Transfer*, vol. 1, no. 2-3, pp. 173-191, 1960.
- [17] C. Gao, "Experimental study on the Ranque-Hilsch vortex tube," 2005.
- [18] B. Ahlborn, J. Keller, and E. Rebhan, "The heat pump in a vortex tube," *Journal of Non-Equilibrium Thermodynamics*, vol. 23, no. 2, pp. 159-165, 1998.

- [19] B. K. Ahlborn and J. M. Gordon, "The vortex tube as a classic thermodynamic refrigeration cycle," *Journal of applied physics*, vol. 88, no. 6, pp. 3645-3653, 2000.
- [20] B. Ahlborn and S. Groves, "Secondary flow in a vortex tube," *Fluid Dynamics Research*, vol. 21, no. 2, p. 73, 1997.
- [21] M. O. Hamdan, S.-A. Al-Omari, and A. S. Oweimer, "Experimental study of vortex tube energy separation under different tube design," *Experimental Thermal and Fluid Science*, vol. 91, pp. 306-311, 2018.
- [22] B. Parulekar, "The short vortex tube," *Journal of refrigeration*, vol. 4, no. 4, pp. 74-80, 1961.
- [23] P. Promvong and S. Eiamsa-ard, "Investigation on the vortex thermal separation in a vortex tube refrigerator," *Science Asia*, vol. 31, no. 3, pp. 215-223, 2005.
- [24] K. Dincer, S. Baskaya, and B. Uysal, "Experimental investigation of the effects of length to diameter ratio and nozzle number on the performance of counter flow Ranque–Hilsch vortex tubes," *Heat and Mass Transfer*, vol. 44, no. 3, pp. 367-373, 2008.
- [25] S. Mohammadi and F. Farhadi, "Experimental analysis of a Ranque–Hilsch vortex tube for optimizing nozzle numbers and diameter," *Applied Thermal Engineering*, vol. 61, no. 2, pp. 500-506, 2013.
- [26] A. Celik, M. Yilmaz, M. Kaya, and S. Karagoz, "The experimental investigation and thermodynamic analysis of vortex tubes," *Heat and Mass Transfer*, vol. 53, no. 2, pp. 395-405, 2017.
- [27] M. O. Hamdan, A. Alawar, E. Elnajjar, and W. Siddique, "Experimental analysis on vortex tube energy separation performance," *Heat and mass transfer*, vol. 47, no. 12, pp. 1637-1642, 2011.
- [28] V. Kırmacı, "Exergy analysis and performance of a counter flow Ranque–Hilsch vortex tube having various nozzle numbers at different inlet pressures of oxygen and air," *International Journal of Refrigeration*, vol. 32, no. 7, pp. 1626-1633, 2009.
- [29] H. R. Thakare and A. D. Parekh, "Experimental investigation of Ranque–Hilsch vortex tube and techno–Economic evaluation of its industrial utility," *Applied Thermal Engineering*, vol. 169, p. 114934, 2020.
- [30] H. Kaya, O. Uluer, E. Kocaoğlu, and V. Kırmacı, "Experimental analysis of cooling and heating performance of serial and parallel connected counter-flow Ranque–Hilsch vortex tube systems using carbon dioxide as a working fluid," *International Journal of Refrigeration*, vol. 106, pp. 297-307, 2019.
- [31] N. Aljuwayhel, G. Nellis, and S. Klein, "Parametric and internal study of the vortex tube using a CFD model," *International journal of refrigeration*, vol. 28, no. 3, pp. 442-450, 2005.
- [32] A. M. Alsaghir, M. O. Hamdan, and M. F. Orhan, "Evaluating velocity and temperature fields for Ranque–Hilsch vortex tube using numerical simulation," *International Journal of Thermofluids*, vol. 10, p. 100074, 2021.
- [33] H. Skye, G. Nellis, and S. Klein, "Comparison of CFD analysis to empirical data in a commercial vortex tube," *International journal of refrigeration*, vol. 29, no. 1, pp. 71-80, 2006.
- [34] M. Baghdad, A. Ouadha, and Y. Addad, "Effects of kinetic energy and conductive solid walls on the flow and energy separation within a vortex tube," *International Journal of Ambient Energy*, pp. 1-17, 2018.

- [35] R. Shamsoddini and A. H. Nezhad, "Numerical analysis of the effects of nozzles number on the flow and power of cooling of a vortex tube," *International journal of refrigeration*, vol. 33, no. 4, pp. 774-782, 2010.
- [36] M. Baghdad, A. Ouadha, O. Imine, and Y. Addad, "Numerical study of energy separation in a vortex tube with different RANS models," *International journal of thermal sciences*, vol. 50, no. 12, pp. 2377-2385, 2011.
- [37] K. Dincer, S. Baskaya, B. Uysal, and I. Ucgul, "Experimental investigation of the performance of a Ranque–Hilsch vortex tube with regard to a plug located at the hot outlet," *International journal of refrigeration*, vol. 32, no. 1, pp. 87-94, 2009.
- [38] A. Secchiaroli, R. Ricci, S. Montelpare, and V. D'alessandro, "Numerical simulation of turbulent flow in a Ranque–Hilsch vortex tube," *International Journal of Heat and Mass Transfer*, vol. 52, no. 23-24, pp. 5496-5511, 2009.
- [39] U. Behera *et al.*, "CFD analysis and experimental investigations towards optimizing the parameters of Ranque–Hilsch vortex tube," *International Journal of Heat and Mass Transfer*, vol. 48, no. 1, pp. 1961-1973, 2005.
- [40] T. Dutta, K. Sinhamahapatra, and S. Bandyopdhyay, "Comparison of different turbulence models in predicting the temperature separation in a Ranque–Hilsch vortex tube," *international journal of refrigeration*, vol. 33, no. 4, pp. 792-783 . 2010
- [41] H. R. Thakare and A. Parekh, "Computational analysis of energy separation in counter—flow vortex tube," *Energy*, vol. 85, pp. 62-77, 2015.
- [42] A. Bramo and N. Pourmahmoud, "A numerical study on the effect of length to diameter ratio and stagnation point on the performance of counter flow vortex tube," *Aust. J. Basic & Appl. Sci*, vol. 4, no. 10, 2010.
- [43] S. Eiamsa-ard and P. Promvong, "Numerical investigation of the thermal separation in a Ranque–Hilsch vortex tube," *International Journal of Heat and Mass Transfer*, vol. 50, no. 5-6, pp. 821-832, 2007.
- [44] T. Farouk, B. Farouk, and A. Gutsol, "Simulation of gas species and temperature separation in the counter-flow Ranque–Hilsch vortex tube using the large eddy simulation technique ", *International Journal of Heat and Mass Transfer*, vol. 52, no. 13-14, pp. 3320-3333, 2009.
- [45] H. Khazaei, A. R. Teymourtash, and M. Malek-Jafarian, "Effects of gas properties and geometrical parameters on performance of a vortex tube," *Scientia Iranica* ,vol. 19, no. 3, pp. 454-462, 2012.
- [46] M. O. Hamdan, B. Alsayyed, and E. Elnajjar, "Nozzle parameters affecting vortex tube energy separation performance," *Heat and Mass Transfer*, vol. 49, no. 4, pp. 533-541, 2013.
- [47] C. Ansys, "Solver theory guide ", *Ansys CFX Release*, vol. 11, pp. 1996-2006, 2006.
- [48] M. Saidi and M. Valipour, "Experimental modeling of vortex tube refrigerator," *Applied thermal engineering*, vol. 23, no. 15, pp. 1971-1980, 2003.
- [49] Y. A. Cengel, *Fluid mechanics*. Tata McGraw-Hill Education, 2010.
- [50] Y. Cengel and T. M. Heat, *A practical approach*. New York, NY, USA: McGraw-Hill, 2003.

Vita

Ahmad Mohammad Alsaghir was born 1994, in Tyre, Lebanon. He was educated at UNRWA private school and graduated from Deir Yassin secondary school in 2012. After that he studied Mechanical engineering at Beirut Arab university and graduate as valedictorian student in 2017.

Mr. Ahmad Moved to United Arab Emirates in 2019 and began a master's program at the American university of Sharjah. He specialized in the field of Thermofluid sciences and their applications in renewable energy.